NATIONAL ADVISORY COMMITTEE FOR AERONAUTICS

TECHNICAL NOTE 3709

AERODYNAMIC INVESTIGATION OF A PARABOLIC BODY OF REVOLUTION AT MACH NUMBER OF 1.92 AND SOME EFFECTS OF AN ANNULAR SUPERSONIC JET EXHAUSTING FROM THE BASE

By Eugene S. Love

Langley Aeronautical Laboratory
Langley Field, Va.

Washington
September 1956

NATIONAL ADVISORY COMMITTEE FOR AERONAUTICS

TECHNICAL NOTE 3709

AERODYNAMIC INVESTIGATION OF A PARABOLIC BODY OF REVOLUTION AT MACH NUMBER OF 1.92 AND SOME EFFECTS OF AN ANNULAR SUPERSONIC JET EXHAUSTING FROM THE BASE[1]

By Eugene S. Love

SUMMARY

An aerodynamic investigation of a parabolic body of revolution was conducted at a Mach number of 1.92 with and without an annular supersonic jet exhausting from the base. Measurements with the jet inoperative were made of lift, drag, pitching moment, radial and longitudinal pressure distributions, and base pressures. With the jet in operation, measurements were made of the pressures over the rear of the body with the primary variables being angle of attack, ratio of jet velocity to free-stream velocity, and ratio of jet pressure to stream pressure.

The results with the jet inoperative showed that the radial pressures over the body varied appreciably from the distribution generally employed in most approximate theories. The linearized solutions for lift, pitching moment, and center of pressure gave relatively poor predictions of the experimental results. An analysis of several theoretical methods for calculating pressure distribution and wave drag showed that some methods gave results in considerable disagreement with experimental values.

Maximum effects of the jet were obtained at the lower ratio of jet velocity to stream velocity and the highest ratio of jet pressure to stream pressure. These effects amounted to a slight decrease in fore-drag, a reduction in lift, and a shift of center of pressure in a destabilizing direction.

INTRODUCTION

Aerodynamic investigations at supersonic speeds of bodies of revolution simulating those containing jet-propulsion units have almost entirely neglected the effects of the jet flow upon the flow over the rear of the body. An experimental subsonic investigation of the effects

---

[1]Supersedes recently declassified NACA Research Memorandum L9K09 by Eugene S. Love, 1950.

of the jet upon the aerodynamic characteristics of the aggregate A-5 missile (body plus four equally spaced tail surfaces) was conducted in Germany in 1940. (See ref. 1.) The results of these tests showed the jet to cause (1) an increase of as much as 100 percent in the normal forces at small angles of attack, (2) a shift of center of pressure to the rear by an average of about 0.5 maximum body diameter, and (3) an increase of drag of approximately 70 percent. Other investigations, both subsonic and supersonic, of jet effects upon the flow over bodies were conducted with the A-4 missile at an angle of attack of 0°. (See ref. 2.) The results of subsonic drag tests were in general agreement with those found in tests of the A-5 missile. The jet caused an increase of drag of as much as 80 percent. The results of the supersonic tests showed a maximum decrease of drag of 18 percent.

In most instances, the best aerodynamic design of bodies housing jet units entails a certain degree of boattailing; that is, convergence of the body surface as it approaches the jet exit. Boattailing such that the diameters of the jet exit and of the exterior body surface become equal would probably favor greater jet effects upon the flow over the rear of the body than would other geometric conditions; therefore, it was chosen as the geometric condition to be employed in the present investigation.

The primary purpose of the investigation was to determine the effects of an annular supersonic jet exhausting from the base of a parabolic body of revolution upon the flow over the rear of the body. It was necessary to obtain first the aerodynamic characteristics of the body without the jet. Therefore, comprehensive force and pressure-distribution measurements were made of the basic jet model body. Similar but not as exhaustive auxiliary tests were conducted on a parabolic body (same body family but larger thickness ratio) initially employed during bench tests of small annular nozzles developed for use in the present investigation. All tests were conducted in the Langley 9-inch supersonic tunnel at a Mach number of 1.92. The Reynolds numbers for the tests were 2.51×10^6 for the jet model body and 2.47×10^6 for the auxiliary body.

SYMBOLS

A, B constants in equation of parabola defining body shapes (eq. (1))

α angle of attack

$\beta = \sqrt{M^2 - 1}$

C_D total drag coefficient $\left(\frac{\text{Drag}}{qS_{max}}\right)$

$C_{D_{min}}$ minimum drag coefficient

C_{D_b} base drag coefficient $\left(P_b \frac{S_b}{S_{max}}\right)$

C_{D_F} minimum foredrag coefficient $\left(C_{D_{min}} - \left(C_{D_b}\right)_{\alpha=0^\circ}\right)$

C_{D_f} skin-friction drag coefficient $\left(C_{f_{lam}} \frac{S_W}{S_{max}}\right)$

C_{D_W} wave-drag coefficient

$C_{f_{lam}}$ skin-friction coefficient for laminar flow on a flat plate $\left(\frac{1.328}{\sqrt{R}}\right)$

C_L total lift coefficient $\left(\frac{\text{Lift}}{qS_{max}}\right)$

c_l weighted unit lift

C_m pitching-moment coefficient $\left(\frac{\text{Moment about reference point}}{qS_{max}l_c}\right)$

d_{max} maximum body diameter

δ lift density

ϵ apex half-angle of body

l body length

l_c cutoff body length

l_t completed body length (tip to tip)

M free-stream Mach number

M_{des} design jet Mach number based on area ratio

η angle of local-surface inclination with respect to axis of symmetry

θ radial angle

p_a atmospheric pressure

p_e static pressure of jet at jet exit

p_s stream pressure or pressure of ambient air

p_{o_m} pressure in model stilling chamber

Δp pressure increment

P pressure coefficient $\left(\frac{\Delta p}{q}\right)$

P_b base pressure coefficient

P_l lifting-pressure coefficient

q dynamic pressure $\left(\frac{1}{2}\rho V^2\right)$

ρ density of fluid

r radius of body

R Reynolds number referred to l_c

S_b base area

S_m mean cross-sectional area for body of length l_c

S_{max} maximum frontal area

S_w wetted area of body of length l_c

t thickness ratio $\left(\frac{d_{max}}{l_t}\right)$

v_{l_c} volume for cutoff body length

v_{l_t} volume for completed body length

V undisturbed stream velocity

V_j velocity of jet

x longitudinal coordinate

Subscripts:

max maximum

L=0 value at zero lift

APPARATUS AND TESTS

Wind Tunnel and Model Installation

The Langley 9-inch supersonic tunnel is a closed-return direct-drive tunnel in which the pressure and humidity of the enclosed air may be controlled. Throughout the tests the quantity of water vapor in the tunnel air was kept at sufficiently low values so that negligible effects on the flow from condensation were present in the supersonic nozzle. The test Mach number is varied by means of interchangeable nozzle blocks forming test sections approximately 9 inches square. A schlieren optical system provides qualitative visual flow observations. Eleven fine-mesh turbulence-damping screens are installed in the settling chamber ahead of the nozzles.

Figure 1 shows the general installation for tests of the jet model. Pressure within the model stilling chamber was varied by means of manually controlled valves installed ahead of the juncture of the incoming-air-supply line with the flexible-air-supply line. Force and pressure-distribution measurements of the models with jet inoperative employed the same model support system with the air-supply system removed. The scales used are self-balancing beam scales and measure three components, in a horizontal plane, of the total forces on the model and support system.

Description of Models

All models were constructed of mild steel, were highly polished, and, except for a special pressure-distribution model, were mounted on slender, hollow sting supports which, for the jet model, served also as an air-supply conduit. The surface contours of the models were determined by revolving about its chord a parabolic arc obtained from the general parabolic equation

$$r = Ax - Bx^2 \tag{1}$$

In this equation the constants A and B can be easily obtained for desired values of maximum diameter, base (or jet-exit) diameter, and thickness ratio. (See appendix.)

Three separate models were constructed with a surface contour given by

$$r = 0.1827x - 0.01854x^2 \tag{2}$$

The designations assigned these models were: model 1-J, the basic jet model with two interchangeable tail sections containing jet nozzles of $M_{des} = 2.11$ (nozzle 1) and $M_{des} = 3.19$ (nozzle 2); model 1-F, the model employed in the force tests; and model 1-P, a special pressure-distribution model constructed in two halves about a meridian plane and containing 63 pressure orifices located in one-half of the model along three meridians, 0°, 45°, and 90°, with 21 orifices similarly spaced along each meridian.

The auxiliary model tested had a surface contour given by

$$r = 0.2460x - 0.02647x^2 \tag{3}$$

This model was designated model 2.

Except for model 1-P, the bases of all the models were hollow or open, as for the case of a jet exit. Special plugs were made to fill the annular base openings of models 1-F and 2 flush with the body ends for use in tests of these models with a simulated solid or closed base. Photographs of models 2, 1-J, and 1-P are shown in figure 2. Model 1-F has been excluded since its external appearance is no different from that of model 1-J.

The following table gives the pertinent geometric parameters of the models:

Parameter	Model 1	Model 2
l_c, in.	7.719	7.607
l_t, in.	9.854	9.293
t	0.09135	0.1230
ϵ, deg	10.36	13.83
v_{l_c}, cu in.	3.113	4.857
v_{l_t}, cu in.	3.346	5.080
S_w, sq in.	16.339	20.330
S_m, sq in.	0.4036	0.6385
S_b, sq in.	0.2923	0.3526
S_{max}, sq in.	0.6365	1.0272
d_{max}, in.	0.9002	1.1436

Development of Annular Nozzles

Numerous bench tests were conducted to determine suitable shapes and sizes of annular nozzles that might be constructed in the tail section of model 1-J. Design of a theoretically shock-free annular supersonic nozzle contour of such small size was not attempted in view of the analytical complications, boundary-layer effects, and the difficulty of machining to the desired accuracy a curving, internal contour of such small radii. Nozzle 2 ($M_{des} = 3.19$) represented the best attempt at construction without prohibitive surface imperfections of a nozzle with a curving contour to give the jet a flow direction at the exit similar to that of nozzle 1 ($M_{des} = 2.11$). In spite of extreme care, small imperfections in the surface contour of this nozzle could be detected. Because of insufficient pressure of the air-supply facility, conclusive bench tests of nozzle 2 could not be made. The higher ratios of p_e/p_s (ratio of jet static pressure to pressure of ambient air) obtainable for nozzle 1 allowed reasonably conclusive bench tests of this nozzle. Diametrical surveys at the nozzle exits were conducted by means of a 0.010-inch total-pressure tube mounted in a micrometer traversing arrangement. The total-pressure tube measured pressures on a plane perpendicular to the nozzle center line and just beyond the nozzle lip. Static pressure within the jet was measured by means of an orifice vented to the nozzle just inside the lip. The Mach number distribution across the nozzle exits was calculated from these pressures with the assumption of negligible effects due to the slight difference in longitudinal positions of the static- and total-pressure measurements and the assumption that the static pressure across the jet was constant. For the values of p_e/p_s of the bench

tests, a conically shaped nozzle was found to give the most uniform distribution at the jet exit for a design Mach number of 2.11. Figures 3(a) and 3(b) show the results of nozzle surveys from bench tests and from tests conducted in a similar manner with the use of the tunnel as a partly evacuated container for the model to obtain larger values of p_e/p_s. The surveys using the tunnel as a vacuum chamber ($p_s \approx 0.6p_a$ in fig. 3(a) and $p_s \approx 0.5p_a$ in fig. 3(b)) show a marked improvement in the distribution for nozzle 2 and a slight lessening of the "hump" in the distribution curve for nozzle 1. The marked improvement in the distribution for nozzle 2 is apparently a result of the decrease in the pressure rise across the shock originating at the lip of the nozzle and reflected by the sting surface, and a decrease in the boundary-layer buildup caused by back pressure which in turn tends to eliminate compressions in the flow within the nozzle. In the bench tests of certain of the annular nozzles of $M_{des} = 3$ or greater ($p_s = p_a$), the large pressure rise across the shock from the lip caused a thickening of the boundary layer near the lip of the outer nozzle surface and a region of reverse flow that extended a considerable distance away from the inner (sting) surface. For the cases for which reverse flow could not be detected, the results indicated that the large adverse pressure rise across the shock caused a rapid thickening of the boundary layer along the sting surface ahead of the point of reflection of the shock. The adverse pressure gradients and the thickening boundary layers probably caused compressions in the flow ahead of the shock and a resulting rapid drop in velocity at the outer and, particularly, the inner diametrical stations. (See fig. 3(b).) With the decrease in external pressure ($p_s \approx 0.5p_a$) the pressure rise across the shock from the lip decreases; therefore, the adverse effects would also be expected to decrease in a manner similar to that indicated in figure 3(b). By similar reasoning, a satisfactory Mach number distribution would be expected at the exit of nozzle 2 in the tunnel tests at $M = 1.92$ for which $p_s \approx 0.14p_a$.

Pressure measurements indicated that the best position for the orifice measuring the pressure in the model stilling chamber p_{o_m} was that shown in figure 1. Thermocouple measurements showed that the temperature of the air in the model stilling chamber varied very little from storage-tank air temperature. Values of the reference pressure p_{o_m} for the jet tests were measured by means of a large Bourdon gage. An open-tube manometer, used in conjunction with this gage, served as a constant check of the pressure gage and supplied values of p_{o_m} for pressures less than atmospheric. Figure 4 shows the calibration curves for each nozzle with the tunnel in operation. Although the values of p_{o_m} were intended to serve only as accurate reference pressures, figures 4 and 5 show that they have some quantitative value as well. The values of Mach number calculated from values of p_e/p_{o_m} and presented

in figure 4 for nozzles 1 and 2 compare favorably with the average values of the Mach number distributions of figures 3(a) and 3(b), respectively. In addition, figure 5 shows that the thrust of nozzle 1 obtained at two values of p_{o_m}/p_a by calculations based upon p_{o_m} and the Mach number distribution checks closely the thrust measured by strain-gage apparatus during the bench tests.

Tests

All tests were conducted through an angle-of-attack range of approximately $\pm 5^{\circ}$. Mirrors approximately 1/16 inch square were flush mounted in the bodies near the base as a part of the optical angle-of-attack system. Force tests and base-pressure measurements of models 1-F and 2 were made with base open and base closed for three longitudinal positions of the models. These were body base even with, 1/2 inch ahead of, and 1 inch ahead of the end of the sting windshield. All drag values were corrected for the buoyancy effect due to the difference between free-stream pressure and the pressure within the box enclosing the sting windshield and balance. Radial and longitudinal surface-pressure measurements were made with model 1-P at meridian intervals of $22\frac{1}{2}^{\circ}$ along every meridian from 0° to $112\frac{1}{2}^{\circ}$ and at 180° (0° to 180° represents angle-of-attack plane). With the jet in operation, the base of the model was 1 inch from the end of the sting windshield. The primary variables of the jet tests were α, p_e/p_s, and V_j/V. For the measurements of the jet effects upon the pressures over the rear of the body, the tubes were installed as shown in the inset in figure 1. Previous investigations showed that the lead tubes in such an arrangement had no measurable effect upon the pressures over the body along a meridian 180° opposite. All schlieren photographs were taken with the knife edge horizontal.

Precision of Data

The estimated probable errors in the aerodynamic quantities are included in the following table. The value of $\pm 0.08^{\circ}$ given for angle of attack is a result of error in the initial referencing of the model bodies with respect to stream direction. The value of $\pm 0.01^{\circ}$ is the error that might be incurred in relative angle-of-attack readings for a given test. The values for C_L, C_D, and C_m apply only to the results obtained from the mechanical scales.

C_L	C_D	C_m	M	α, deg		R	P
				Initial	Relative		
±0.0004	±0.0004	±0.0018	±0.01	±0.08	±0.01	±20,000	±0.002

Comparison of the actual ordinates of the model bodies with the values obtained from equations (2) and (3) showed the body dimensions to be accurate, with one exception, within ±0.002 inch. This exception, the tail section of model 1-J containing nozzle 1, had gradually increasing small errors in the radii of the body from a point approximately 0.3 inch from the base rearward. The maximum error in radius (at the body base) amounted to ±0.008 inch. The effects of this lesser degree of boat-tailing will be shown in the results. The meridian planes and rotational angles for the radial pressure distributions were accurate within ±2°. The Bourdon gage for measuring p_{o_m} gave readings accurate within ±0.2 pound per square inch.

RESULTS AND DISCUSSION

Jet Inoperative

Force tests.- Figure 6 shows the aerodynamic characteristics of model 1-F for the three longitudinal positions of the model in relation to the forward tip of the sting windshield. Corresponding schlieren photographs for these and two additional positions are shown in figure 7. In like manner, the aerodynamic characteristics of model 2 and schlieren photographs at two longitudinal positions are shown in figures 8 and 9, respectively. Except for the zero longitudinal position, all schlieren photographs in figures 7 and 9 were taken at zero angle of attack. Values of C_m in figures 6 and 8 are for moments taken about the point of maximum diameter.

The results of base-pressure measurements with varying longitudinal position and angle of attack indicated much the same effects from the presence of the sting support and windshield and from angle of attack as discussed in references 3, 4, and 5; specifically, the base pressures vary appreciably with angle of attack, and the body undergoing test must be mounted on a long, slender sting support if base pressures simulating free-flight values are to be obtained. The results of the force tests are given in table I.

The condition of the base of the bodies, open or closed, had little or no consistent effect upon the results except a slight increase in the base drag for the closed condition. The values of base drag at the zero longitudinal position of the models are to serve only in establishing the magnitude of the foredrag and not as accurate measurements of the base drag since the proximity of the sting windshield to the body base would affect the base pressures. The effects on the lift and moment curves from the flow impinging upon the exposed sting at the higher angles of attack are shown in figures 6 and 8. These effects increase as the exposed sting area increases and cause marked nonlinearities in the curves. The longitudinal position of the models apparently had little effect on the minimum foredrag coefficient C_{D_F} although close examination of the schlieren photographs in figures 7 and 9 shows a lessening of the laminar separation near the base of the body with increasing distance between the body base and the tip of the sting windshield.

Values of drag coefficient due to skin friction C_{D_f} (laminar flow was observed over the entire body) were calculated for the test Reynolds number. These values and their approximate percentage of the foredrag are presented in the following table:

Model	C_{D_f}	Percent of C_{D_F}
1-F	0.0216	30
2	.0167	14

References 6, 7, and 8 have pointed out independently that at least to first order the limiting value for the lift-curve slope of very slender bodies of revolution at small α is (expressed in radians and based upon S_b)

$$\frac{dC_L}{d\alpha} = 2 \tag{4}$$

and that the center-of-pressure location in relation to the nose of the body is

$$\text{Center of pressure} = 1 - \left(\frac{S_m}{S_b}\right)l \tag{5}$$

From equations (4) and (5) it follows that the slope of the pitching-moment curve, with moments taken about the nose of the body, is

$$\frac{dC_m}{d\alpha} = 2\left(1 - \frac{S_m}{S_b}\right) \tag{6}$$

The values calculated from equations (4), (5), and (6), expressed in degrees and referred to S_{max}, are presented in the following table and compared with the experimental values (in parentheses) obtained at the 1-inch longitudinal position. The experimental values of lift-curve and moment-curve slopes given in table I include support interference effects and aerodynamic tares on the exposed sting. However, the experimental slope values are for zero lift, and pressure measurements along a 1-inch length of the exposed sting from the body base have shown the lifting forces upon the sting to be negligible within an angle-of-attack range of $\pm 2^{\circ}$. Furthermore, the effects of the presence of the sting and windshield upon the body lifting forces would be expected to be least at the 1-inch position.

Model	$\frac{dC_L}{d\alpha}$	c.p. (diam. from nose)	$\frac{dC_m}{d\alpha}$ about nose
1-F	0.0160 (.0290)	3.26 (1.28)	-0.00610 (-.00431)
2	.0120 (.0338)	5.49 (1.39)	-.00975 (-.00705)

All the theoretical values are relatively poor predictions of the experimental results. Part of the failure of equations (4), (5), and (6) to predict values in reasonable agreement with experimental values is probably caused by the use of the geometrical value of base area. Reference 3 has shown that the calculated pressures over the rear of a body of revolution with boattailing, as given by the method of characteristics, are in excellent agreement with experimental pressures if the pressure calculations are performed along the streamline of separated boundary layer. This would seem to indicate that the geometrical value of base area in equations (4), (5), and (6) should be replaced by an area determined by the diameter between the separated streamlines at the body base. Measurements of this "diameter of separation" were made from enlarged schlieren photographs of models 1-F and 2, each at the 1-inch longitudinal position and with open base. An area of 0.347 square inch was obtained for model 1-F and an area of 0.474 square inch for model 2. The values

calculated from equations (4), (5), and (6) and referred to these areas are presented in the following table and compared with the experimental values (in parentheses):

Model	$\frac{dC_L}{d\alpha}$	c.p. (diam. from nose)	$\frac{dC_m}{d\alpha}$ about nose
1-F	0.0190 (.0290)	1.40 (1.28)	-0.00310 (-.00431)
2	.0161 (.0338)	2.31 (1.39)	-.00559 (-.00705)

Although these values are an improvement upon the previous theoretical values, they are still rather poor predictions.

Pressure distributions.- The results of radial-pressure-distribution measurements are presented in figure 10 for model 1-P and in figure 11 for model 2. Longitudinal pressure distributions are presented in figures 12 and 13 for model 1-P and in figure 14 for model 2. Radial pressures for model 2 are given in figure 15. Although the results for model 2 are secondary to those for model 1-P, they tend to indicate that certain phenomena observed in the pressure distributions of both bodies apparently hold for slender pointed bodies of revolution in general. First, figures 10, 11, 13(b), 14(c), and 15 show that the pressures along the 90° meridian at $\alpha = 0^\circ$ do not remain relatively unchanged with angle of attack, a simplifying assumption often employed in approximate theories for computing the aerodynamic characteristics of conical bodies and pointed bodies of revolution. In fact, at certain horizontal stations the pressure at the 90° meridian varies as much as or more than at any other meridian. Second, the radial pressure distribution at any longitudinal station varied appreciably from the usually assumed cosine distribution, especially for the low-pressure half of the body at longitudinal stations ahead of the maximum thickness and for the entire circumference at stations behind the maximum thickness. The radial pressures at stations behind the maximum thickness behave in much the same manner as observed in tests of slender cylinders in yaw. (See ref. 9.) Third, for longitudinal stations ahead of the maximum thickness there appears to be a radial point for each longitudinal station at which the pressure remains almost constant with angle of attack. (See fig. 15, in particular.) The locus of these radial points does not follow a meridian but tends to move away from the 90° meridian in the direction of the high-pressure half of the body as the distance from the nose increases. For model 1-P, this shift was from $\theta \approx 80^\circ$ at station 0.088 to $\theta \approx 48^\circ$ at station 0.606. For model 2, the shift was from $\theta \approx 78^\circ$ at station 0.283 to $\theta \approx 61^\circ$ at station 0.573. The fourth phenomenon

observed was the consistent appearance of the "hump," not predicted by potential theory, in the longitudinal-pressure-distribution curves. For model 1-P, this characteristic occurred near the 0.3 station, and for the $\alpha = 0^{\circ}$ condition amounted to a noticeable discontinuity in the curve. For model 2, it occurred in the vicinity of the 0.5 to 0.6 stations. This phenomenon has been present in the results of other tests of slender pointed bodies of revolution (refs. 5 and 10, for example) and, except for cones, is apparently characteristic of slender pointed bodies of revolution in general. Although cross velocities in the vicinity of the 90° meridian would not be expected to affect the lift, their inclusion would, nevertheless, be expected to reduce the pressures at the 90° meridian, possibly of the magnitude observed in the experimental results. Also, when the experimental longitudinal pressure gradients in the vicinity of the 90° meridian are found to be relatively large, the experimental tangential pressure gradients are found to be of the same order of magnitude. A tangential gradient of such magnitude would be expected to have important bearing upon separation effects.

Figure 16 illustrates the method by which the pressure coefficient at any point on the body is converted to the lifting-pressure coefficient P_l. The equation, including second-order terms, is

$$P_l = P(\cos\theta \cos\eta \cos\alpha + \sin\eta \sin\alpha) \tag{7}$$

All values of P for model 1-P were converted to P_l by means of equation (7). With S_{max} as the reference area, the total lift coefficient would be given by (see diagram in upper half of fig. 17)

$$C_L = \frac{1}{S_{max}} \int_0^l \int_0^{2\pi} P_l r \, d\theta \, \frac{1}{\cos\eta} \, dx \tag{8}$$

Plots of $P_l/\cos\eta$ against θ were made for each horizontal station and graphically integrated from 0 to 2π. This gave what might be termed the lift density δ at each station. Therefore, the weighted unit lift for each station x is

$$(c_l)_x = \delta_x r_x \tag{9}$$

From the linear first-approximation theory of reference 7 and the first-order approximation theory of reference 11, a solution for the lift distribution over the body from equation (4) would apparently give an acceptable first-order prediction. In the dimensions of equation (9) and for small values of α, this solution may be expressed as

$$(c_l)_x = 4\alpha\pi r_x\left(\frac{dr}{dx}\right)_x \tag{10}$$

In figure 17 the values of $(c_l)_x$ from equations (9) and (10) are plotted against horizontal station, in inches, for values of α of 2.50° and 5.00°. This gives a graphical representation of the lift distribution over the body. Values of C_L and C_m determined by integration of the experimental curves and the theoretical values (in parentheses) are presented in the following table:

α, deg	C_L	C_m about nose	c.p. (diam. from nose)
2.50	0.0717 (.0400)	−0.00733 (−.01525)	0.88 (3.26)
5.00	.1472 (.0800)	−.0230 (.03050)	1.34 (3.26)

Since the tests of model 1-P most nearly duplicate in tunnel position the tests of model 1-F at the 1-inch longitudinal sting station, a reasonable check of the pressure-distribution results should be realized in a comparison with the force-data results for the 1-inch sting station (open base). In an effort to eliminate as much as possible the effects of the sting support, values based upon the slopes of the curves at zero lift were determined from table I. These values are included in the following table. Of course, the use of constant slopes will mask the effects of separation at the rear of the body.

α, deg	C_L	C_m about nose	c.p. (diam. from nose)	Source
2.50 5.00	0.0725 .1450	−0.0108 −.0216	1.28 1.28	Constant slope Constant slope
2.50 5.00	.0700 .1450	−.00766 −.0146	.94 .86	Average-curve value Average-curve value

Model 1-F was also tested as shown in figure 18. The results are given in figure 19 and in the following table:

α, deg	C_L	C_m about nose	c.p. (diam. from nose)
2.50	0.0860	-0.0246	2.45
5.00	.1831	-.0532	2.49

These values do not show close agreement with the values obtained from model 1-P, but it is interesting to note that they agree closely with the results of the tests of model 1-F, open base, at the zero longitudinal position; thus, an appreciable effect from the flush sting-windshield arrangement is indicated. As might be expected, the only close check of the values obtained through integration of the pressure distributions lies in a comparison at $\alpha = 2.50^{\circ}$ with the average-curve values from tests of model 1-F at the 1-inch longitudinal sting station. On this basis, the results of the pressure-distribution integrations may be considered reliable. The shift of center of pressure with angle of attack, as determined from the pressure distributions, would correspond to effects that might be expected from separation of the flow at the rear of the body.

The results of the pressure-distribution investigations give some insight into the causes of the higher experimental values of $dC_L/d\alpha$, as compared with theoretical values, noted in these and other tests of slender pointed bodies of revolution. Figure 17 shows that, for body stations behind the station at which the theoretical local lift would be a maximum, the experimental values of local lift exhibit a marked increase over the theoretical values. The station of initial gain in the experimental local lift also appears to be in the region where the experimental radial pressures begin to deviate appreciably from a cosine distribution. It is seen that the observed noncosine distributions of radial pressures act in such a way as to give more lift over the body than would cosine distributions. Figure 17 also shows the expected reduction of antilift forces by separation in the region over the rear of the body where recompression would otherwise take place.

Analysis of theoretical methods for prediction of longitudinal pressure distribution.- The equations for several methods for predicting the pressure distribution over slender pointed bodies of revolution were calculated in terms of equation (1). Reference 8 gives a solution termed the "rigorous linearized first-order solution" for an extremely sharp nose body of revolution for $M > \sqrt{2}$. This yields

$$P \approx -2(A^2 - 6ABx + 6B^2x^2)\log(A - Bx) \tag{11}$$

which was obtained in reference 8 from a previously derived equation for the pressure coefficient for compressible flow, given herein as

$$P = -A^2 + 16ABx - 22B^2x^2 + 2(A^2 - 6ABx + 6B^2x^2)\left[\log 2 - \log(\beta A - \beta Bx)\right] +$$

$$O(A^3 - 3A^2Bx + 3AB^2x^2 - B^3x^3) \tag{12}$$

By the method of reference 12, but with axes at the nose of the body, the general equation was found to be

$$P = 2\left\{(6AB - 9B^2x)\sqrt{x^2 - \beta^2r^2} + \left[A^2 - 6ABx + 3B^2(2x^2 + \beta^2r^2)\right]\cosh^{-1}\frac{x}{\beta r}\right\} \tag{13}$$

Reference 13 gives a solution for P that is identical with equation (13) except for one additional term. This solution is

$$P = \text{Value from equation (13)} - (A^2 - 4ABx + 4B^2x^2) \tag{14}$$

Reference 10 has given a solution based upon the small-disturbance theory and requiring a step-by-step numerical integration. For simplicity this method will be expressed herein merely as

$$P = \sum_{i=1}^{n}\left[f(r,M)\right] \tag{15}$$

where i and n represent the initial and nth integration station, respectively. A 25-point calculation was made. The final method employed was the characteristics method of references 14 and 15 with the assumption of potential flow.

Equations (11) to (15) were applied to the body shapes of models 1 and 2. The characteristics method was applied to model 1 only. The results of these pressure-distribution calculations are presented in figure 20. The corresponding wave drag coefficients C_{D_W} from integration of the pressure curves are given in the following table:

Method	Model 1	Model 2
Equation (11)	0.0253	0.0356
Equation (12)	.0784	.1498
Equation (13)	.0822	.1548
Equation (14)	.0740	.1302
Equation (15)	.0746	.1309
Characteristics method	.0624	------

Integration of a curve determined by the experimental points of figure 20 gives for model 1 a pressure-drag coefficient of 0.0542 and for model 2 a drag of 0.11. (This value is very approximate because of lack of sufficient points.) It should be noted that no correction has been applied to the experimental points since surveys have shown only minor variation in the static-pressure distribution in the wind-tunnel test section. Therefore, any correction applied to the pressure drag would be minor. The effects of separation upon the experimental pressure-drag coefficient would not oppose the indication that all these theories predict too large a wave drag. As might be expected, the characteristics method shows best agreement with experiment. Although it gives only a fair prediction, equation (14), the Lighthill solution, is the best of the approximate theories and gives a slightly better prediction of the experimental results than does the laborious small-disturbance method of equation (15). Indications are that equation (11) should not be applied.

If the values of the experimental pressure drag are assumed to approach the wave drag, the addition of the laminar skin-friction drag should give a value that checks closely the measured foredrag. The comparison is given in the following table. The corresponding values of the foredrags are from table I, 1-inch position, open base.

Model	Experimental pressure drag plus C_{D_f}	Foredrag from force tests
1	0.0758	0.0743
2	.1267	.1104

Jet in Operation

Figure 21 presents schlieren photographs of the jet model with and without tubes to the pressure orifices installed as shown in the upper left-hand corner of figure 1. As previously stated, pressure measurements with no jet throughout the angle-of-attack range showed no effect upon the body pressures from the presence of or disturbances produced by the pressure lead tubes on the side of the body opposite the pressure orifices. The surveys and calibrations of the two jet nozzles indicated reasonable values of the Mach numbers for the two jet nozzles to be approximately 2.10 and 3.05. For a free-stream Mach number of 1.92, these values would represent ratios of jet velocity to stream velocity V_j/V of approximately 1.05 and 1.24, respectively.

Figure 22 shows the pressure change at each orifice location due to jet effects with varying jet pressure and angle of attack. Also included are the hysteresis effects (at the $\alpha = 0^\circ$ and $\alpha = 2.50^\circ$, upper surface, for both velocity ratios) dependent upon whether the particular test was made with increasing or decreasing jet pressures. For both velocity ratios the major effects upon the pressures over the rear of the body occurred at $\alpha = 0^\circ$ and $\alpha = 2.50^\circ$, upper surface, and were confined to the orifices nearest the jet exit. At these α conditions and a velocity ratio of 1.05, the body pressures increased positively as the jet pressure approached and exceeded stream pressure, the greatest change occurring immediately after the over-pressure condition $\frac{p_e}{p_s} > 1$ was reached. At the same α conditions and a velocity ratio of 1.24, the body pressures showed a very slight decrease at the under-pressure conditions $\frac{p_e}{p_s} < 1$ and a slight increase at the over-pressure conditions. At $\alpha = 5.00^\circ$ the jet had no significant effect at either velocity ratio. Figure 23 gives the percentage change in body pressures due to the jet at $\alpha = 0^\circ$ and $\alpha = 2.50^\circ$, upper surface, for several values of p_e/p_s. At the top of the figure the differences in the basic pressure distributions over the rear of model 1-P and the two nozzle tail sections (no jet) of model 1-J are presented for $\alpha = 0^\circ$. These differences in pressures appear to be the effects of previously mentioned very small measured differences in body ordinates. The zero-percent datum lines of the plots of jet effects represent the pressures with no jet. The major effects of the jet upon the body pressures are confined to approximately 5 percent of the body length (from the base) for a velocity ratio of 1.24 and to approximately 10 percent of the body length for a velocity ratio of 1.05. For similar pressure ratios p_e/p_s the effect of the jet upon

the body pressures in these regions is much greater for the lower velocity ratio. At $\alpha = 2.50^{\circ}$, upper surface, there is a positive increase in jet effects over the $\alpha = 0^{\circ}$ condition. This might be expected in view of the greater separation of the flow from the upper surface at angle of attack that would favor pressure effects from the jet to be felt farther forward along the body and to a greater degree.

Typical schlieren photographs of the jet in operation at $\alpha = 0^{\circ}$ are shown in figure 24 for the two velocity ratios and, whenever possible, for similar pressure ratios. Photographs at the lower velocity ratio were taken with the lead tubes installed; therefore, for comparison with the photographs at the higher velocity ratio which were taken without the tubes installed, the simple pattern of disturbances present in the jet-inoperative photograph should be ignored.

As the supersonic jet begins to flow, there is a decrease in thickness of the laminar boundary layer at the rear of the body. This is particularly true at the higher velocity ratio. Up to a value of p_e/p_s equal to approximately 0.5, the shock pattern within the jet and at the nozzle lip is much the same for both velocity ratios. A very prominent lambda shock is noted at the jet outer boundary immediately rearward of the nozzle lip. The shock pattern within the jet follows closely the expected phenomena for under-pressure jets calling for the presence of a shock to offset the higher pressure outside the jet boundary. From $\frac{p_e}{p_s} = 0.5$ to 1.0, the lambda shock at the jet outer boundary tends toward a plain shock whose apparent point of origin at the jet boundary lies slightly downstream of the nozzle lip. The shock pattern within the jet continues along the pattern for under-pressure jets except that two shocks are now observed within the jet of higher velocity ratio. It is possible that this may be due to slight imperfections in the nozzle surface; but, in view of the fact that a similar phenomenon, though not as strong, may be observed at slightly higher pressure ratios at the lower velocity ratio, it appears more probable that this phenomenon is characteristic of the flow from annular nozzles of this type. At a value of $\frac{p_e}{p_s} \approx 1$, the jet boundaries are parallel to the axis of symmetry of the jet. Parallel flow would not be expected to occur exactly at $\frac{p_e}{p_s} = 1$ because the stream pressure would be somewhat different from the pressure behind the shock emanating from the vicinity of the nozzle lip. Also, the presence of the shocks within the parallel jet at $\frac{p_e}{p_s} \approx 1$ may be attributed to the necessary change in flow inclination from a direction that is away from the axis of symmetry immediately ahead of the exit at the nozzle lip to a direction parallel to the axis of symmetry beyond the exit. At the higher values of p_e/p_s separation occurs at the rear of

the body; this separation is more pronounced at the lower velocity ratio. An expansion of the jet flow occurs at the nozzle lip for the over-pressure conditions $\frac{p_e}{p_s} > 1$ and is followed by shocks within the jet. (See fig. 25.) With increasing over pressures of the jet, the shock from the outer boundary of the jet near the jet exit reverts more and more to a lambda shock at the higher velocity ratio, whereas the corresponding shock at the lower velocity ratio continues as a clearly defined plain shock. Indications from the pressure measurements and the schlieren photographs are that the induced velocities imparted to the semidead air in the region where the flow is separated from the rear of the body are greater for the case of the higher velocity ratio. Apparently, these induction effects tend to counteract the back-pressure effects over the body from the related internal (jet) and external flow characteristics.

The effects of the jet upon the foredrag of the body ($\alpha = 0^{\circ}$) were determined from the measured body pressures. The results are tabulated in the following table as percentage change in C_{D_F}:

p_e/p_s \ V_j/V	1.05	1.24
0.4	0.34	----
1.0	-.21	0.72
1.5	-1.01	0
1.8	-1.62	-.43
3.5	-3.31	----

The maximum effect of the jet upon the lift and pitching moment occurred at $\alpha = 2.50^{\circ}$ and, as in the case for the foredrag, at the lower velocity ratio, 1.05, and highest pressure ratio, 3.5. An approximation of this effect is entered on the curve representing lift distribution in figure 17. The results of such a change in lift distribution would be a 13.7-percent decrease in the overall lift of the body and a destabilizing shift of center of pressure from 0.88 diameter rearward of the nose to a point 0.74 diameter ahead of the nose. Although the foregoing determination of jet effects has assumed the interference effects of the sting and windshield on the pressure measurements to be the same for the jet-on and jet-off conditions, the differences in the effects are expected to be small. Thus, the foregoing values should give an insight into the magnitude of some of the effects that might be expected from an exhausting annular jet.

CONCLUSIONS

An aerodynamic investigation at a Mach number of 1.92 of a parabolic body of revolution with and without a supersonic annular jet exhausting from the base indicates the following conclusions for the case with the jet inoperative:

1. The condition of the base of the body, hollow or closed, has little and no consistent effect upon the aerodynamic characteristics of the body.

2. The simplified linearized solutions for lift-curve slope, pitching-moment-curve slope, and center-of-pressure location give relatively poor predictions of the experimental results.

3. Experimental radial pressure distributions show a marked deviation of lifting pressures from the theoretical cosine distribution, and, contrary to the simplifying assumption of most approximate theories, the pressures on the sides of the body (90° from angle-of-attack plane) vary appreciably with angle of attack. These discrepancies appear to be the result of separation effects and of the failure of the theories to include effects of cross velocities which may be important.

4. The method of characteristics for axial symmetry gives a reasonable overall prediction of the actual pressure distribution over the body. However, a "hump," not predicted by potential theory, is found in the experimental longitudinal-pressure-distribution curve at forward body stations. This phenomenon appears to be characteristic of slender pointed bodies of revolution in general.

5. The Lighthill solution appears to be the best of the linearized solutions investigated for prediction of pressure distribution over slender bodies of revolution.

For the case with the jet in operation, the following conclusions are indicated:

6. Pressures over the rear of the body show little effect from the jet until the jet pressure ratio approaches and exceeds the value for parallel flow of the jet.

7. The effects of the jet upon the body pressures are reduced as the ratio of jet velocity to free-stream velocity increases.

8. The greatest effects of the jet upon the lift and pitching moment occur at 2.50° angle of attack and almost completely disappear as the angle of attack is increased to 5.00°.

9. Maximum effects of the jet are obtained at the lower ratio of jet velocity to stream velocity, 1.05, and the highest ratio of jet pressure to stream pressure, 3.5. These effects amount to a 3.3-percent reduction in foredrag at 0° angle of attack and, at 2.50° angle of attack, a 13.7-percent reduction in lift and a destabilizing shift of center of pressure from 0.88 body diameter rearward of the nose to a point approximately 0.74 diameter ahead of the nose.

10. Indications are that, for higher ratios of jet velocity to stream velocity than achieved in the present investigation, the induction effects of the jet upon the flow over the rear of a body of this type would become as important as the back-pressure effects.

Langley Aeronautical Laboratory,
National Advisory Committee for Aeronautics,
Langley Field, Va., November 25, 1949.

APPENDIX

Body Parameters

The general equation for the shape of the bodies is given as

$$r = Ax - Bx^2 \tag{A1}$$

The constants A and B may be determined simply as follows. At maximum thickness and in nondimensional form

$$\frac{r_{max}}{l} = \frac{A^2}{4Bl} \tag{A2}$$

Also

$$B = \frac{A - \frac{r_{base}}{l}}{l} \tag{A3}$$

If r_{max}, r_{base}, and the thickness ratio are assigned fixed values, the constants A and B are readily obtained by combining equations (A2) and (A3). Examination of the basic equation (A1) shows that the constant A is dimensionless and is equal to twice the thickness ratio. However, the constant B is not dimensionless. Therefore, any calculations employing equation (A1) with the numerical values replacing the constants A and B, such as computations of pressure distributions or drag, must be carried through with the same dimension units (feet or inches) used in calculating the values of A and B.

The following equations apply to the family of bodies determined from equation (A1):

$$\text{Volume} = \pi\left(\frac{A^2l^3}{3} - \frac{ABl^4}{2} + \frac{B^2l^5}{5}\right) \tag{A4}$$

$$\text{Mean area} = \pi\left(\frac{A^2l^2}{3} - \frac{ABl^3}{2} + \frac{B^2l^4}{5}\right) \tag{A5}$$

$$\text{Wetted surface area} = \pi\left(Al^2 - \frac{2}{3}Bl^3\right) \tag{A6}$$

REFERENCES

1. Erdmann: Einfluss des Strahles auf die aerodynamischen Eigenschaften des Aggregats A 5. Archiv Nr. 66/23, Heeres Versuchsstelle, Peenemünde, Mar. 12, 1940.

2. Erdmann: Drag Coefficients of the A4V1P Including Jet and Friction Effects for Sub- and Supersonic Velocities. Investigation of Jet Expansion. Translation No. F-TS-662-RE, Air Materiel Command, U. S. Army Air Forces, Sept. 1946. (From Archiv Nr. 66/105 g. Kdos, Aerodynamisches Institut, Heeres Versuchsstelle, Peenemünde, Mar. 24, 1943.)

3. Chapman, Dean R., and Perkins, Edward W.: Experimental Investigation of the Effects of Viscosity on the Drag and Base Pressure of Bodies of Revolution at a Mach Number of 1.5. NACA Rep. 1036, 1951. (Supersedes NACA RM A7A31a.)

4. Faro, I.: OAL Wind Tunnel Study of a Free Flight Model at a Mach Number of 2.0. Rep. No. CF-812, The Johns Hopkins Univ., Appl. Phy. Lab., Apr. 19, 1948.

5. Ferri, Antonio: Supersonic-Tunnel Tests of Projectiles in Germany and Italy. NACA WR L-152, 1945. (Formerly NACA ACR L5H08.)

6. Munk, Max M.: The Aerodynamic Forces on Airship Hulls. NACA Rep. 184, 1924.

7. Tsien, Hsue-Shen: Supersonic Flow Over an Inclined Body of Revolution. Jour. Aero. Sci., vol. 5, no. 12, Oct. 1938, pp. 480-483.

8. Laitone, E. V.: The Linearized Subsonic and Supersonic Flow About Inclined Slender Bodies of Revolution. Jour. Aero. Sci., vol. 14, no. 11, Nov. 1947, pp. 631-642.

9. Hasel, Lowell E., and Coletti, Donald E.: Investigation of Two Pitot-Static Tubes at Supersonic Speeds. NACA RM L8I02, 1948.

10. Von Kármán, Theodor, and Moore, Norton B.: Resistance of Slender Bodies Moving With Supersonic Velocities, With Special Reference to Projectiles. Trans. A.S.M.E., vol. 54, no. 23, Dec. 15, 1932, pp. 303-310.

11. Lighthill, M. J.: Supersonic Flow Past Slender Pointed Bodies of Revolution at Yaw. Quarterly Jour. Mech. and Appl. Math., vol. 1, pt. 1, Mar. 1948, pp. 76-89.

12. Jones, Robert T., and Margolis, Kenneth: Flow Over a Slender Body of Revolution at Supersonic Velocities. NACA TN 1081, 1946.

13. Lighthill, M. J.: Supersonic Flow Past Bodies of Revolution. R. & M. No. 2003, British A.R.C., 1945.

14. Ferrari, C.: Campo aerodinamico a velocità iperacustica attorno a un solido di rivoluzione a prora acuminata. L'Aerotecnica, vol. XVI, fasc. 2, Feb. 1936, pp. 121-130.

15. Ferri, Antonio: Application of the Method of Characteristics to Supersonic Rotational Flow. NACA Rep. 841, 1946. (Supersedes NACA TN 1135.)

TABLE I.- SUMMARY OF FORCE-TEST RESULTS FOR

MODELS 1-F AND 2 WITH JET INOPERATIVE

Model	Distance from body base to forward end of sting windshield (in.)	Base condition	$\left(\frac{dC_L}{d\alpha}\right)_{L=0}$	$\left(\frac{dC_m}{d\alpha}\right)_{L=0}$ about d_{max}	$C_{D_{min}}$	$\left(C_{D_b}\right)_{\alpha=0^\circ}$	c.p. (diam. from nose)
1-F	0	Open	0.0334	0.0121	0.0899	0.0142	2.37
	0	Closed	.0330	.0124	.0879	.0156	2.25
	.5	Open	.0324	.0126	.0940	.0214	2.14
	.5	Closed	.0323	.0102	.0955	.0233	2.77
	1.0	Open	.0290	.0142	.0960	.0217	1.28
	1.0	Closed	.0292	.0140	.0960	.0235	1.45
2	0	Open	.0392	.0112	.1370	.0217	2.16
	0	Closed	.0394	.0110	.1373	.0220	2.21
	.5	Open	.0427	.0105	.1400	.0241	2.43
	.5	Closed	.0429	.0105	.1400	.0252	2.43
	1.0	Open	.0338	.0136	.1410	.0306	1.39
	1.0	Closed	.0343	.0130	.1407	.0309	1.54

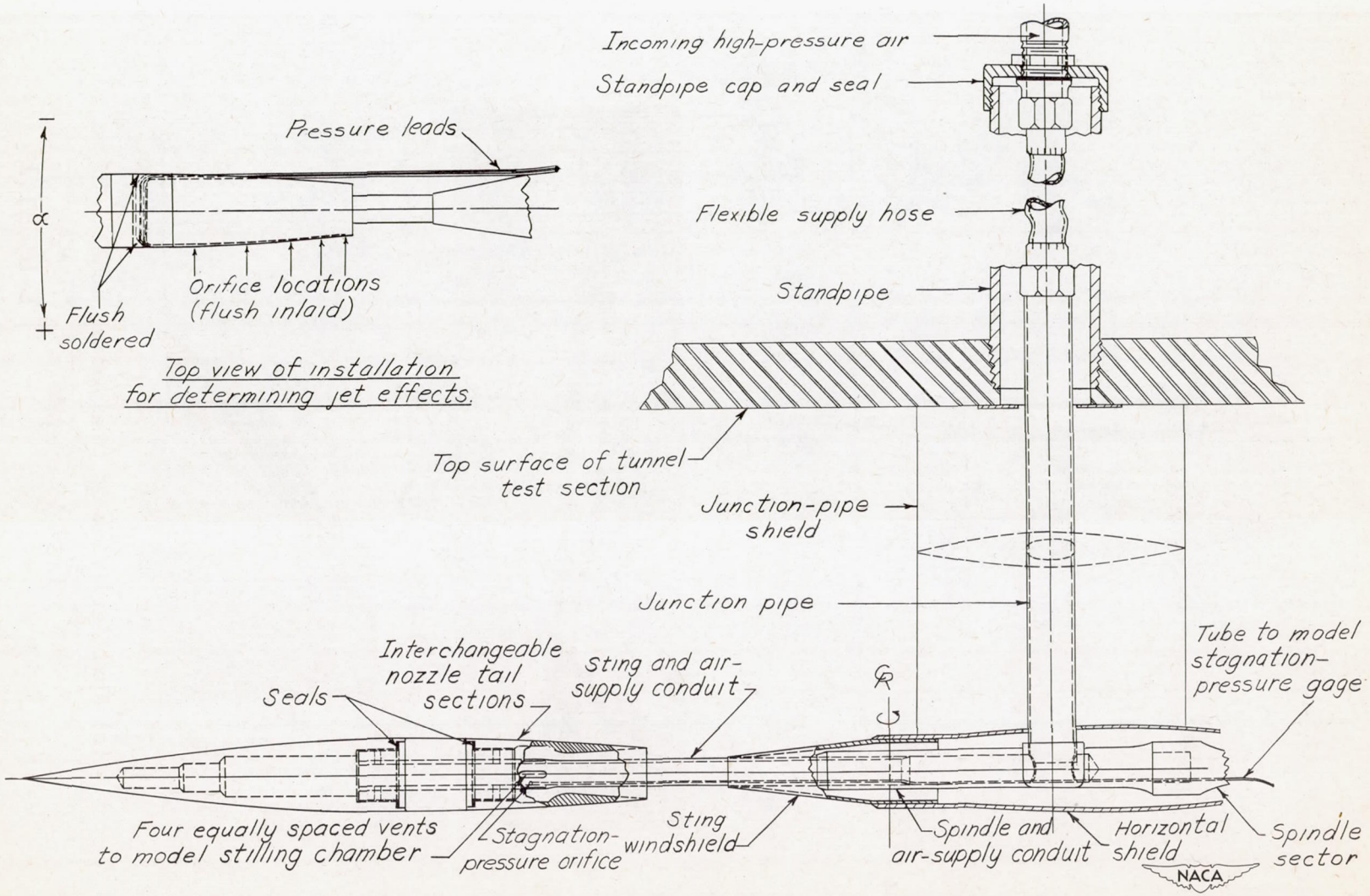

Figure 1.- Tunnel installation for tests of jet model.

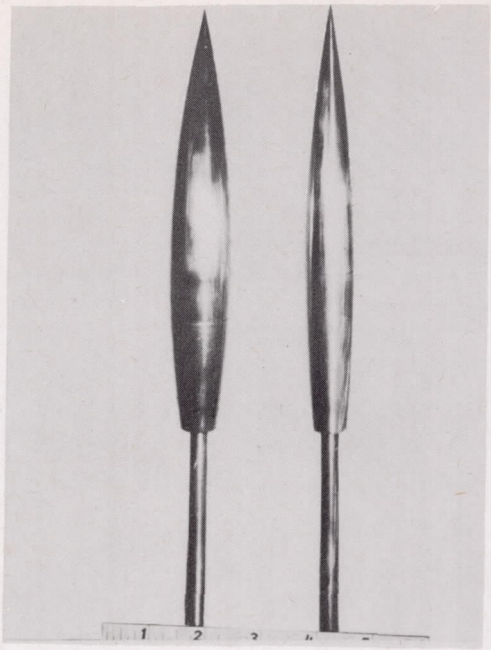

(a) Models 2 and 1-J.

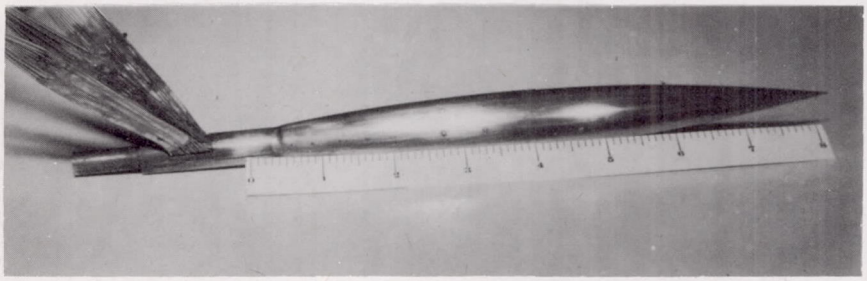

(b) Side view of model 1-P.

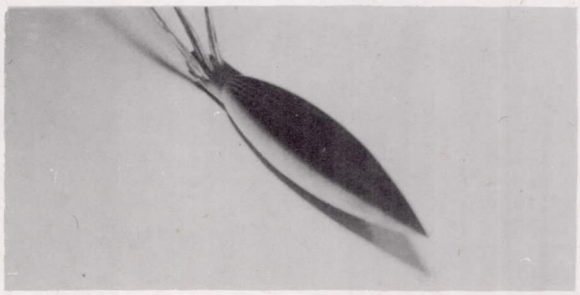

(c) Auxiliary view of tube exits, model 1-P.

Figure 2.- Models.

L-63041.1

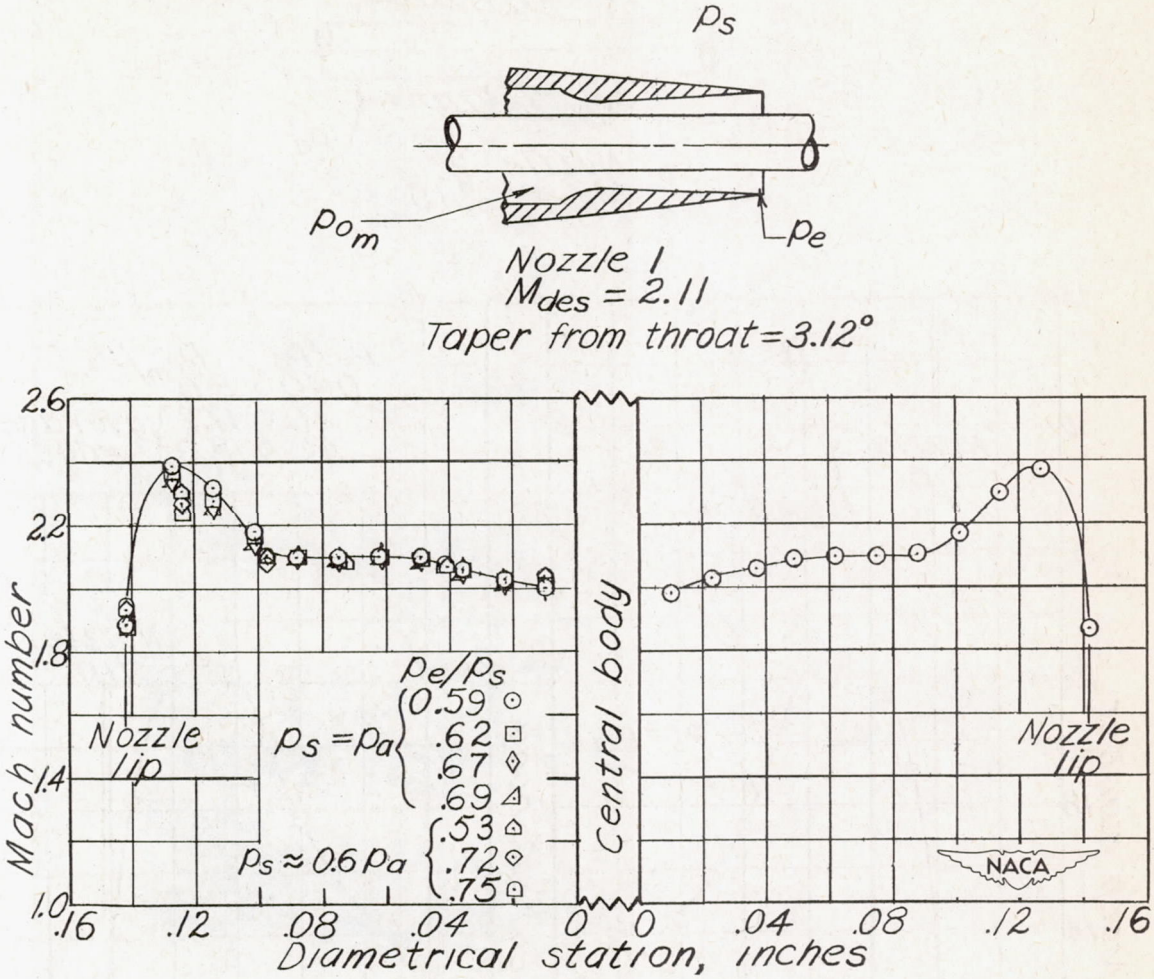

(a) Nozzle 1, M_{des} = 2.11.

Figure 3.- Results of surveys of nozzle exits.

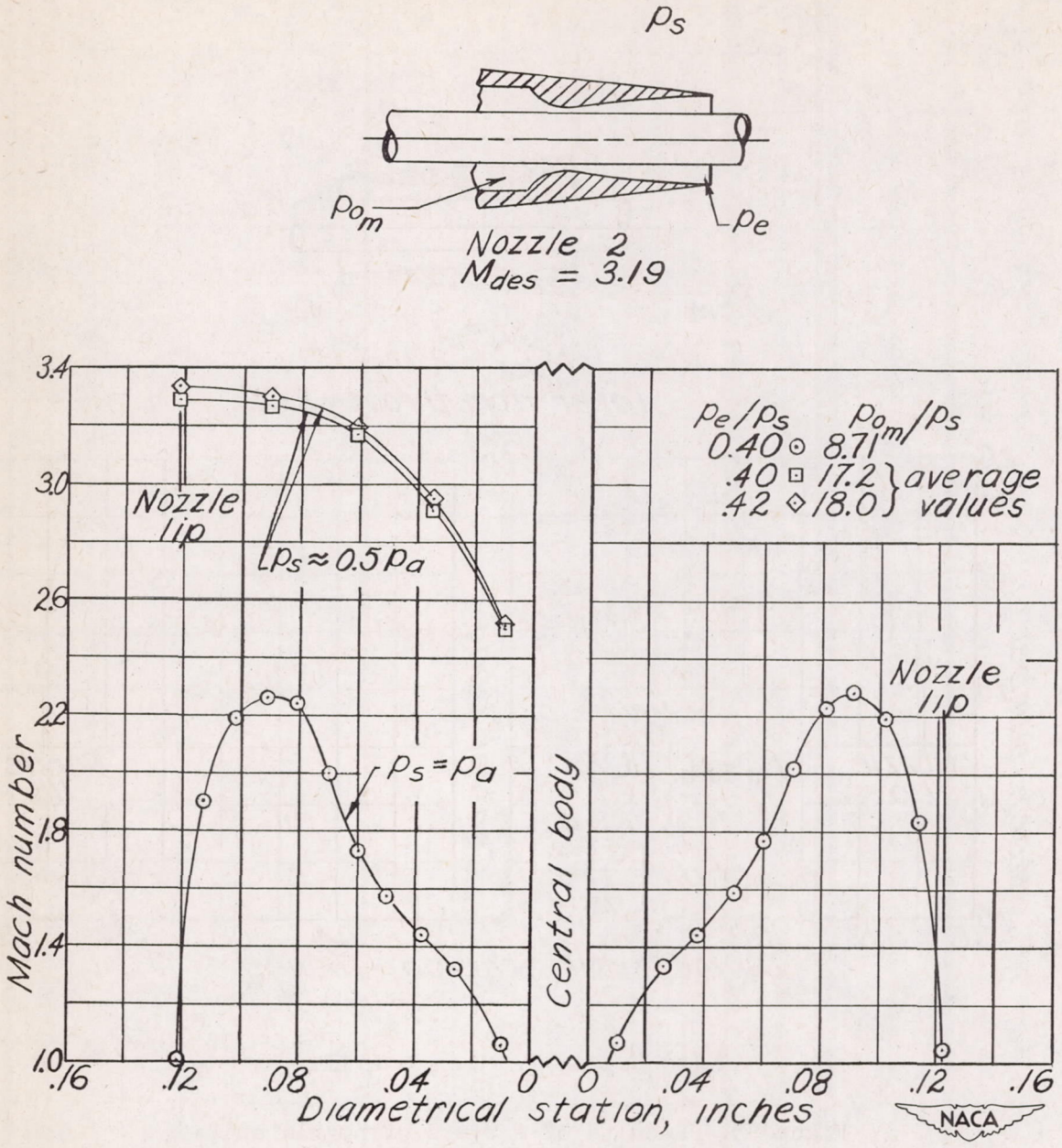

(b) Nozzle 2, M_{des} = 3.19.

Figure 3.- Concluded.

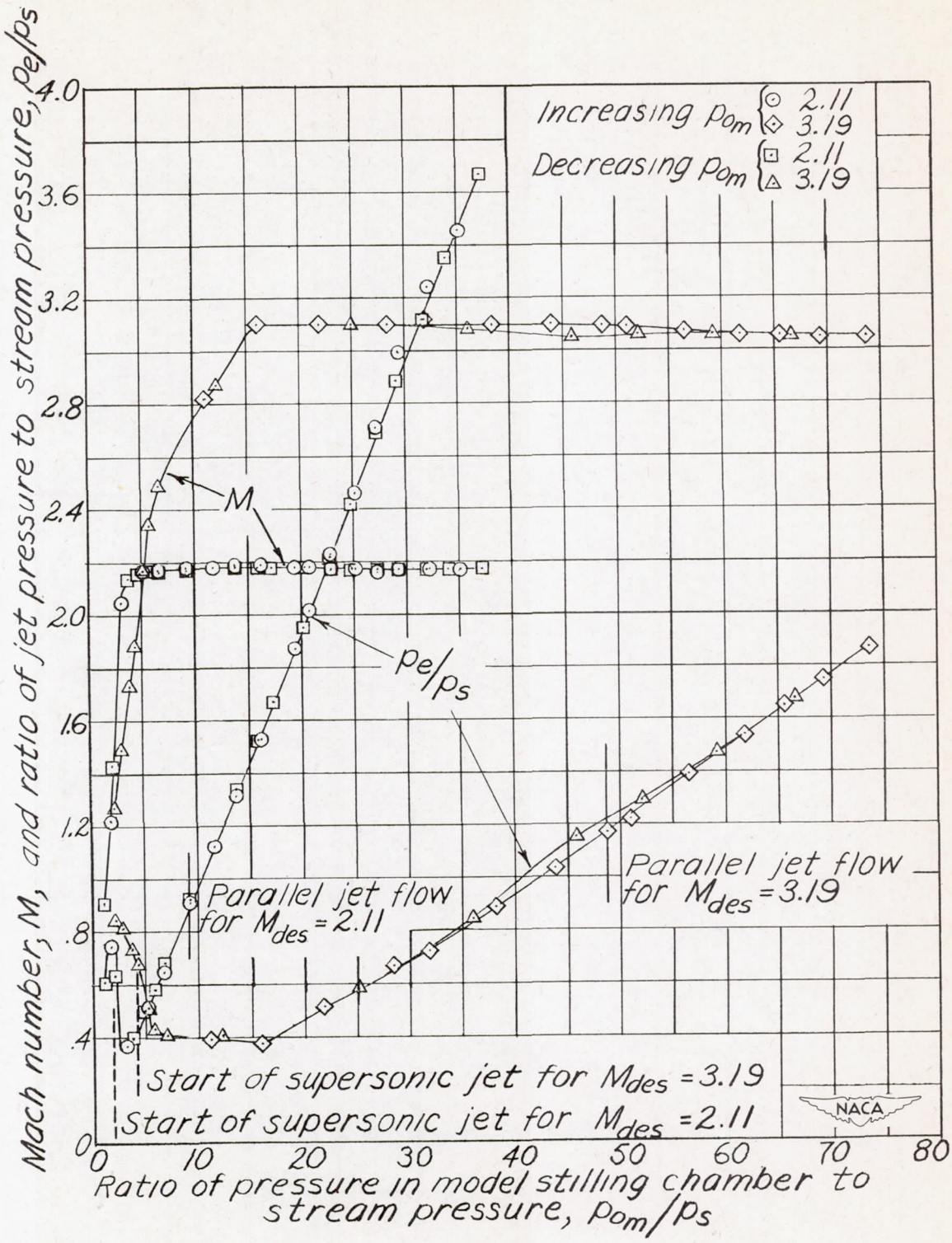

Figure 4.- Calibration of jet nozzles in tunnel.

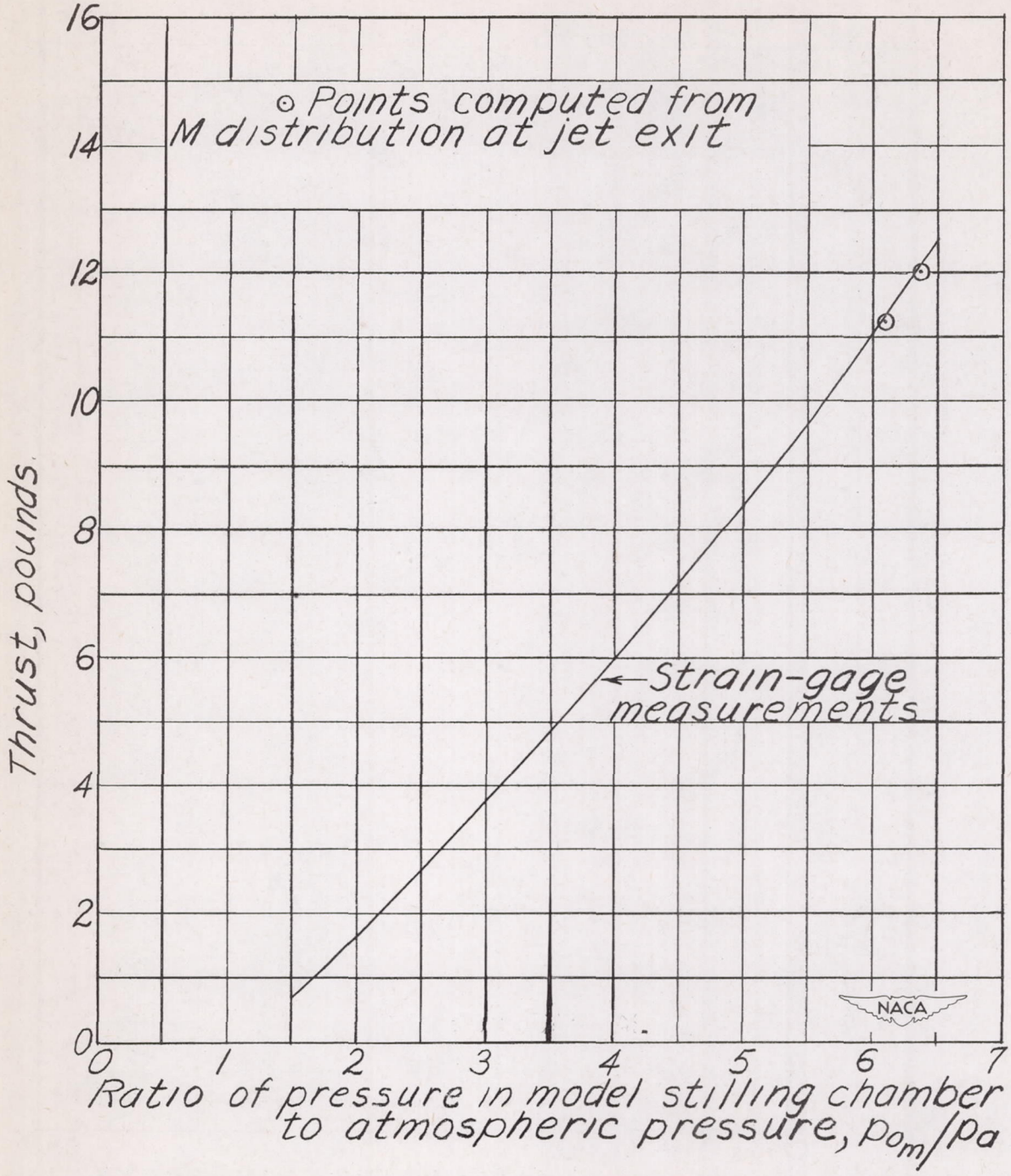

Figure 5.- Thrust of nozzle 1.

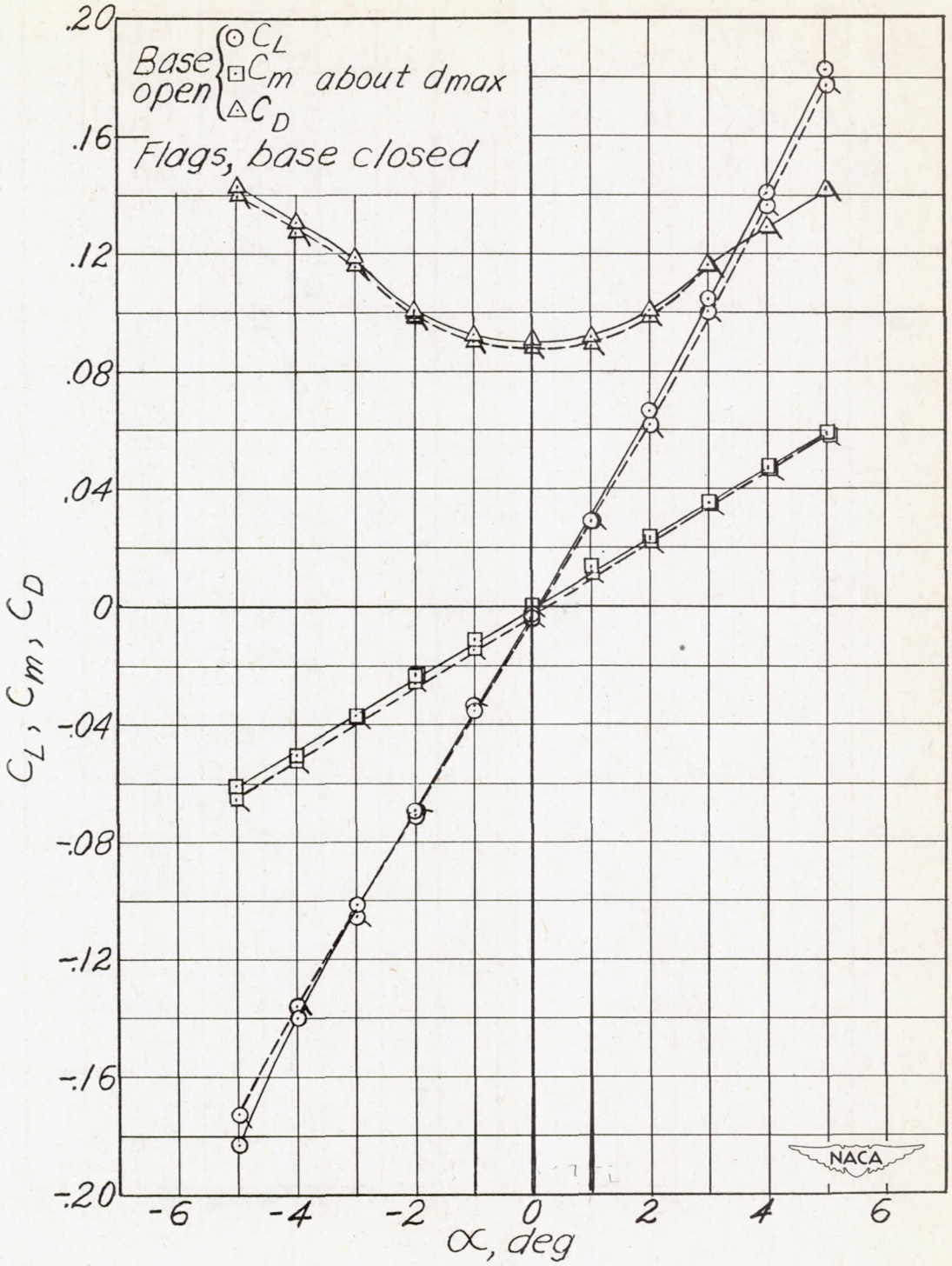

(a) Base to windshield is 0 inch. .

Figure 6.- Aerodynamic characteristics of model 1-F.

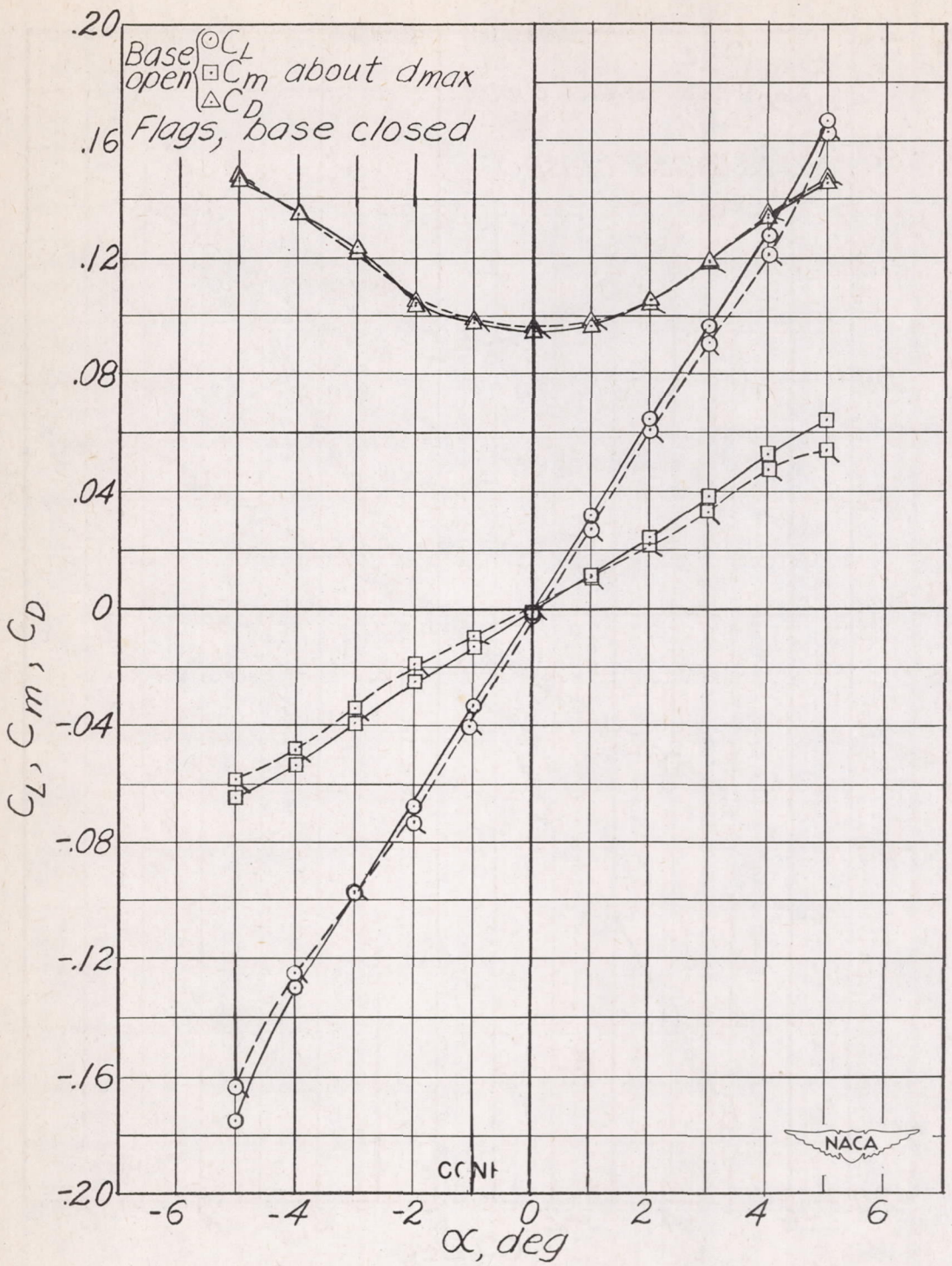

(b) Base to windshield is 0.5 inch.

Figure 6.- Continued.

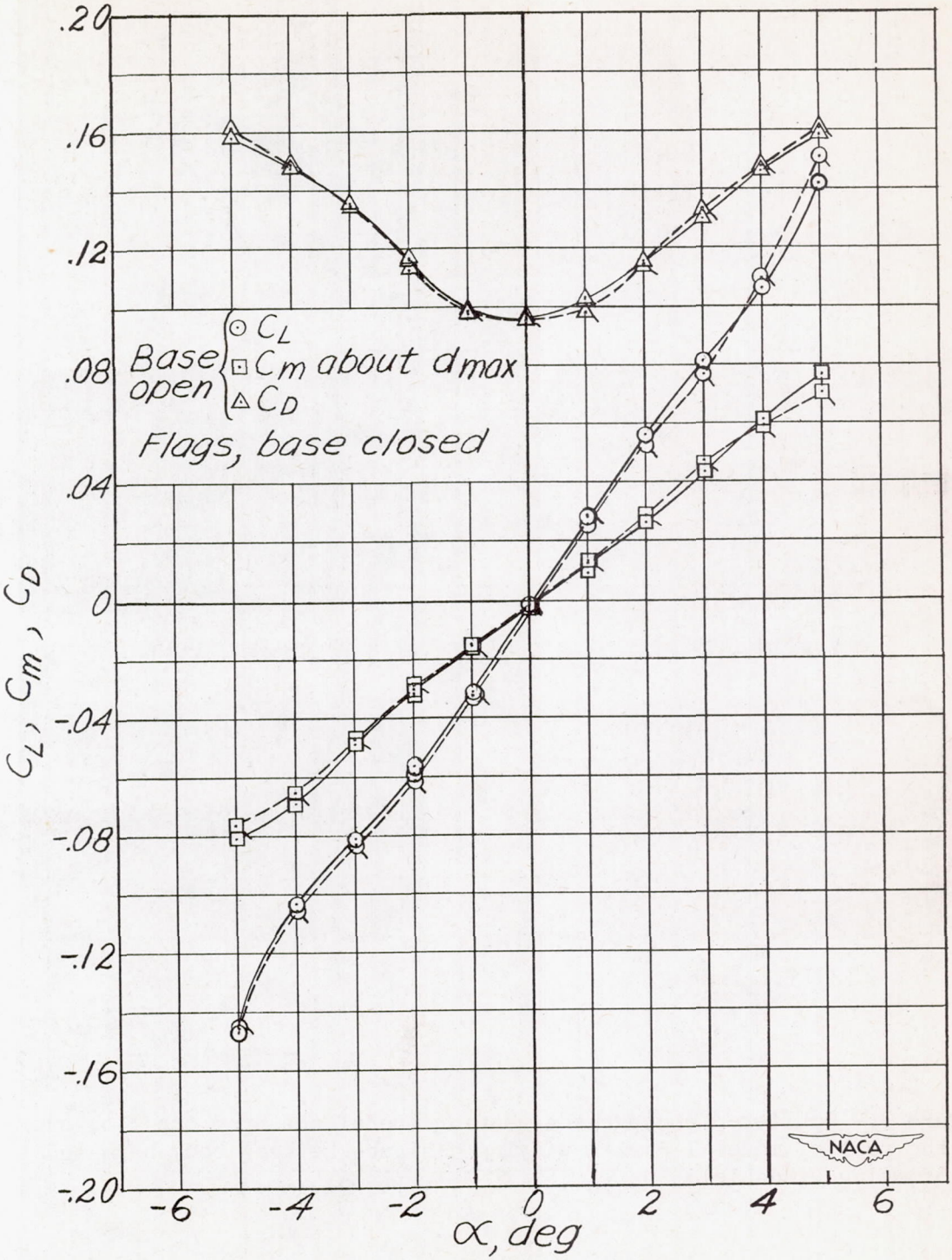

(c) Base to windshield is 1.0 inch.

Figure 6.- Concluded.

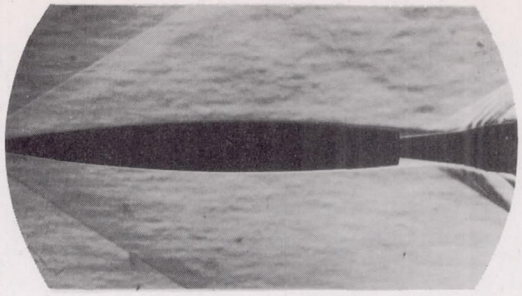

(a) 0 inch.

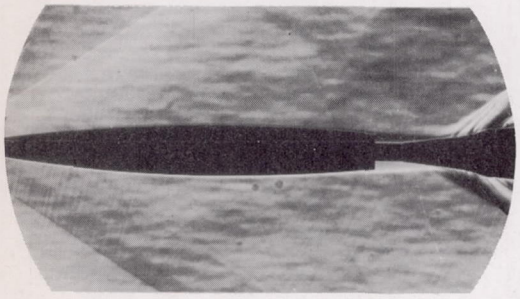

(b) 0.5 inch.

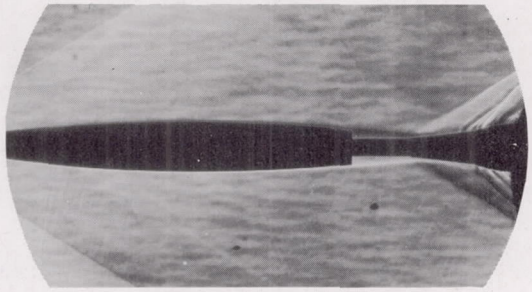

(c) 1 inch.

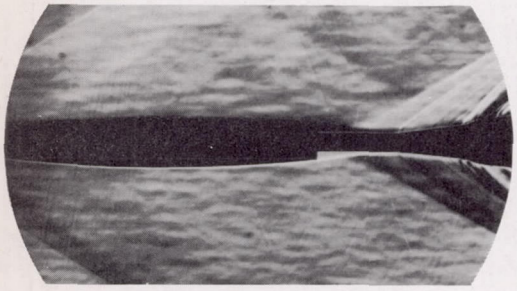

(d) 1.5 inches.

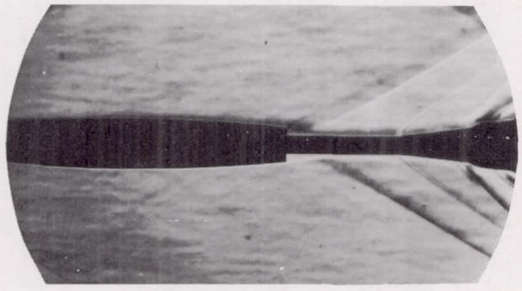

(e) 2 inches.

NACA

L-63042

Figure 7.- Schlieren photographs showing the effect upon the flow over the rear of model 1-F with varying distance between body base and tip of sting windshield.

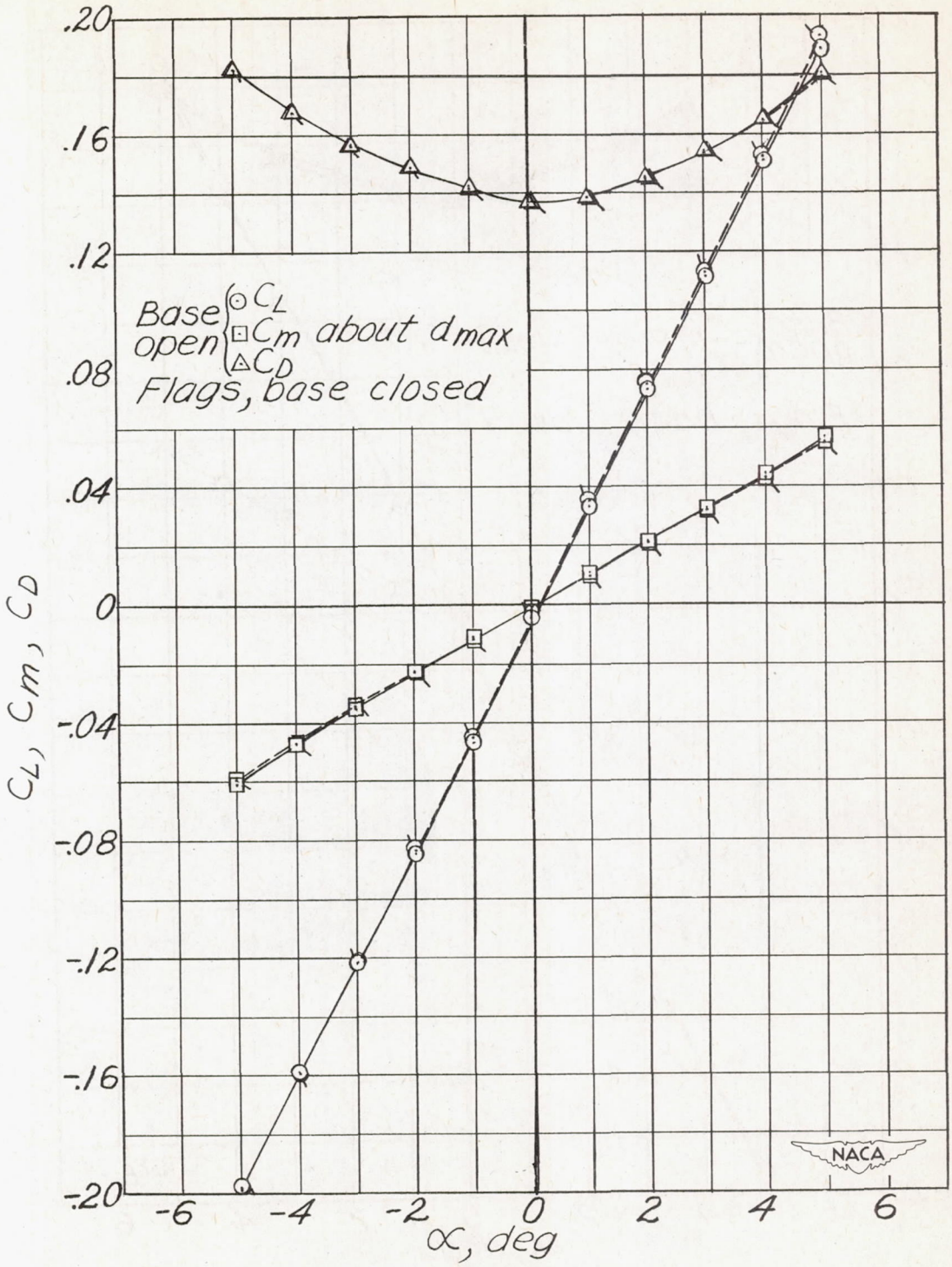

(a) Base to windshield is 0 inch.

Figure 8.- Aerodynamic characteristics of model 2.

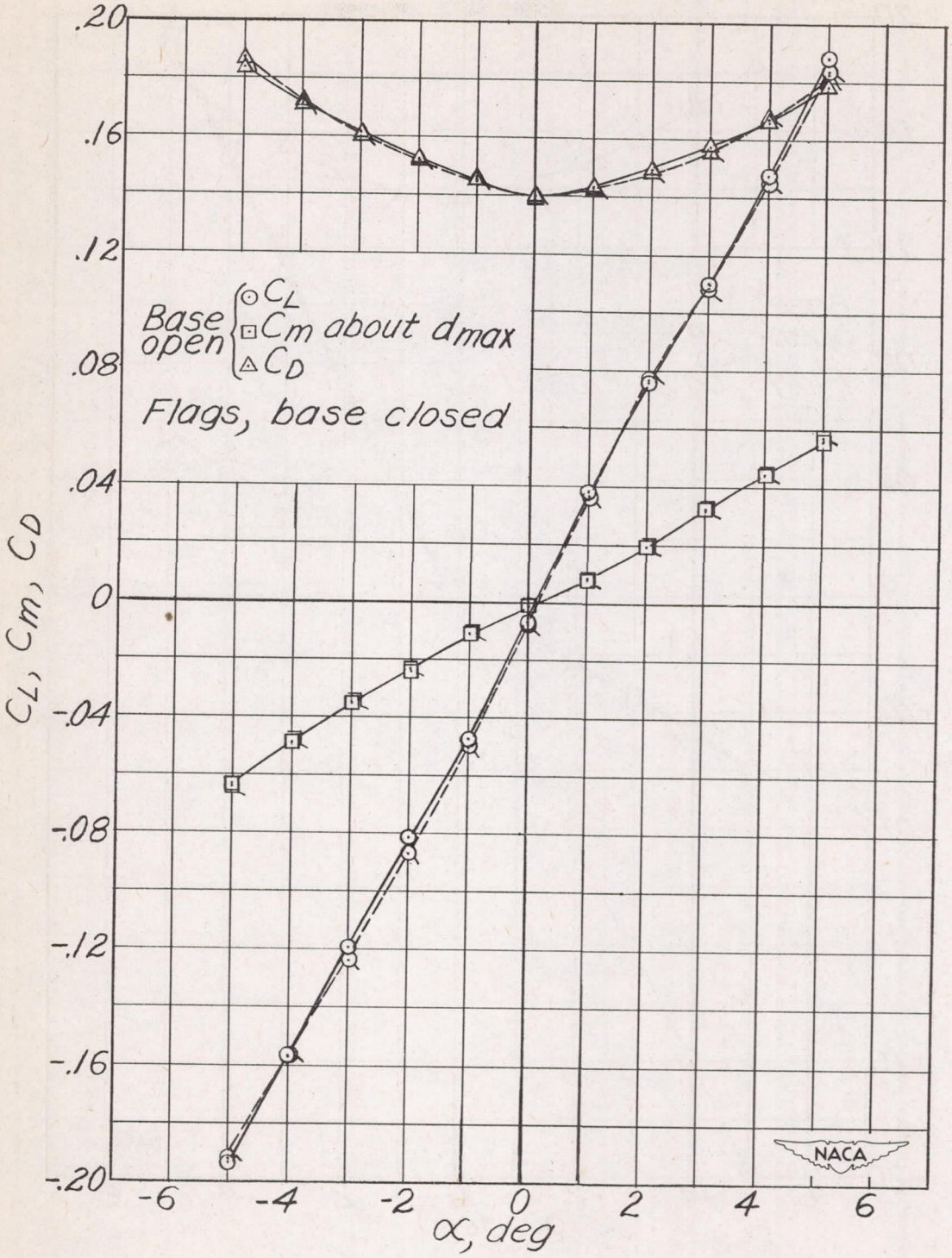

(b) Base to windshield is 0.5 inch.

Figure 8.- Continued.

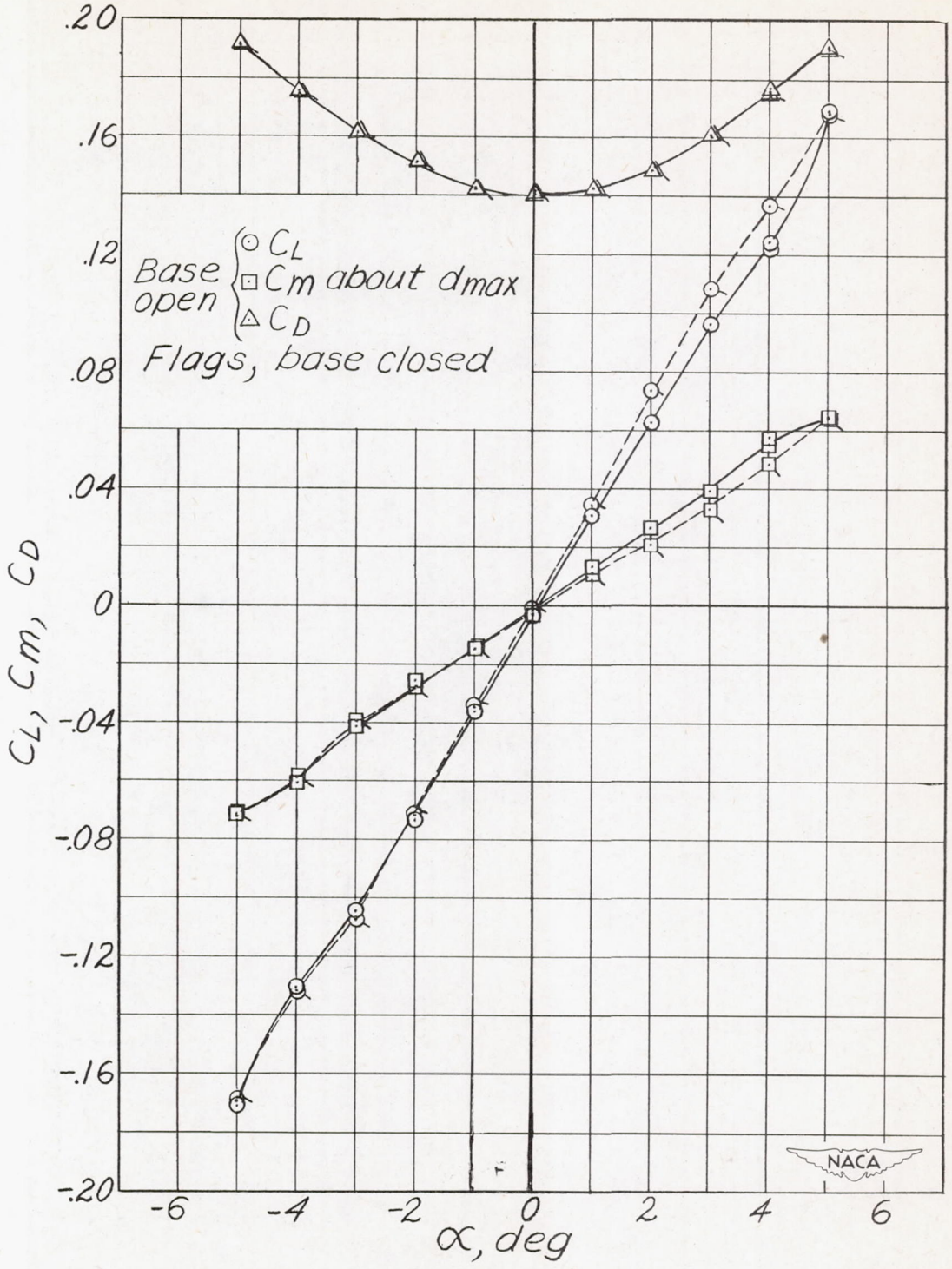

(c) Base to windshield is 1.0 inch.

Figure 8.- Concluded.

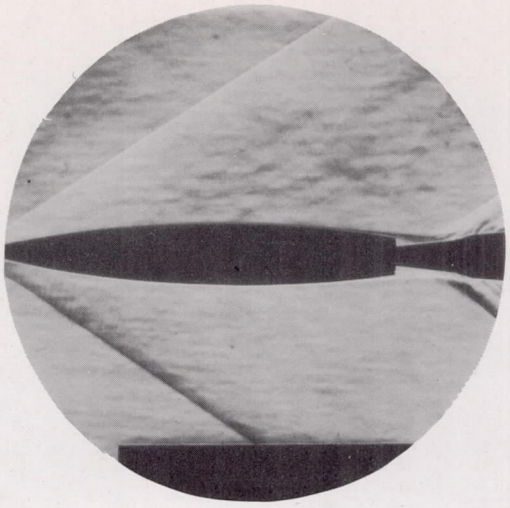

(a) 0 inch.

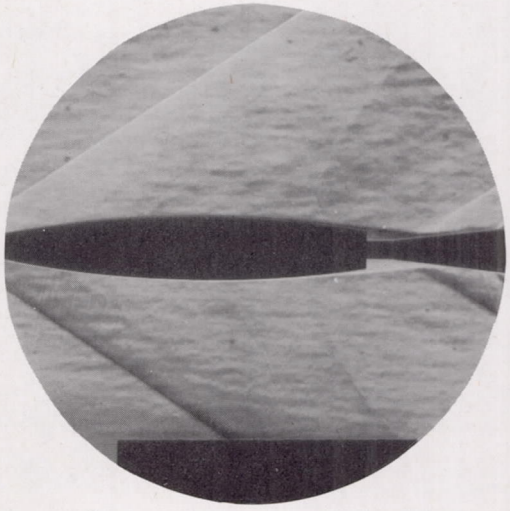

(b) 0.5 inch.

NACA
L-63043

Figure 9.- Schlieren photographs showing the effect upon the flow over the rear of model 2 with varying distance between body base and tip of sting windshield.

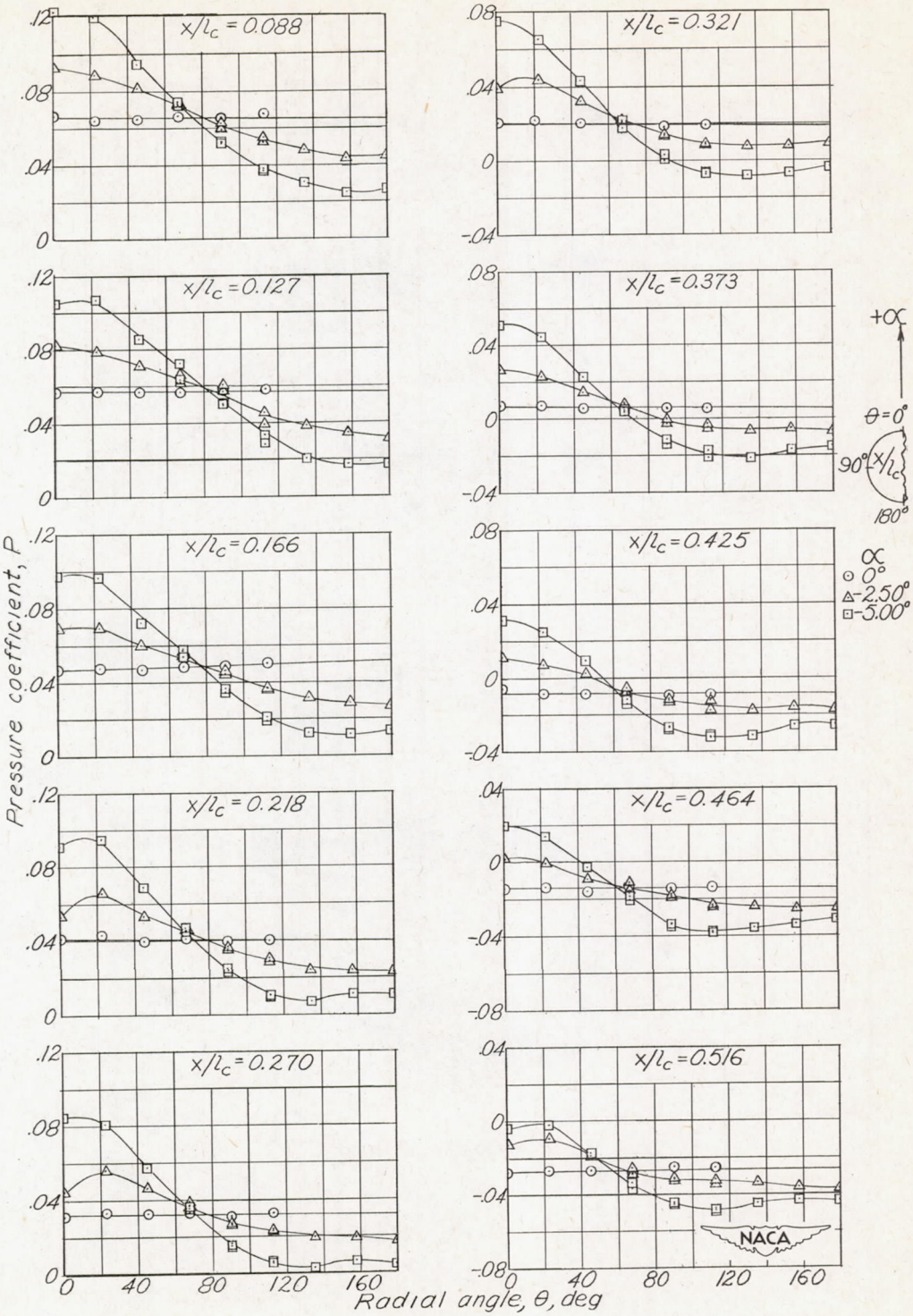

Figure 10.- Radial pressure distributions for model 1-P.

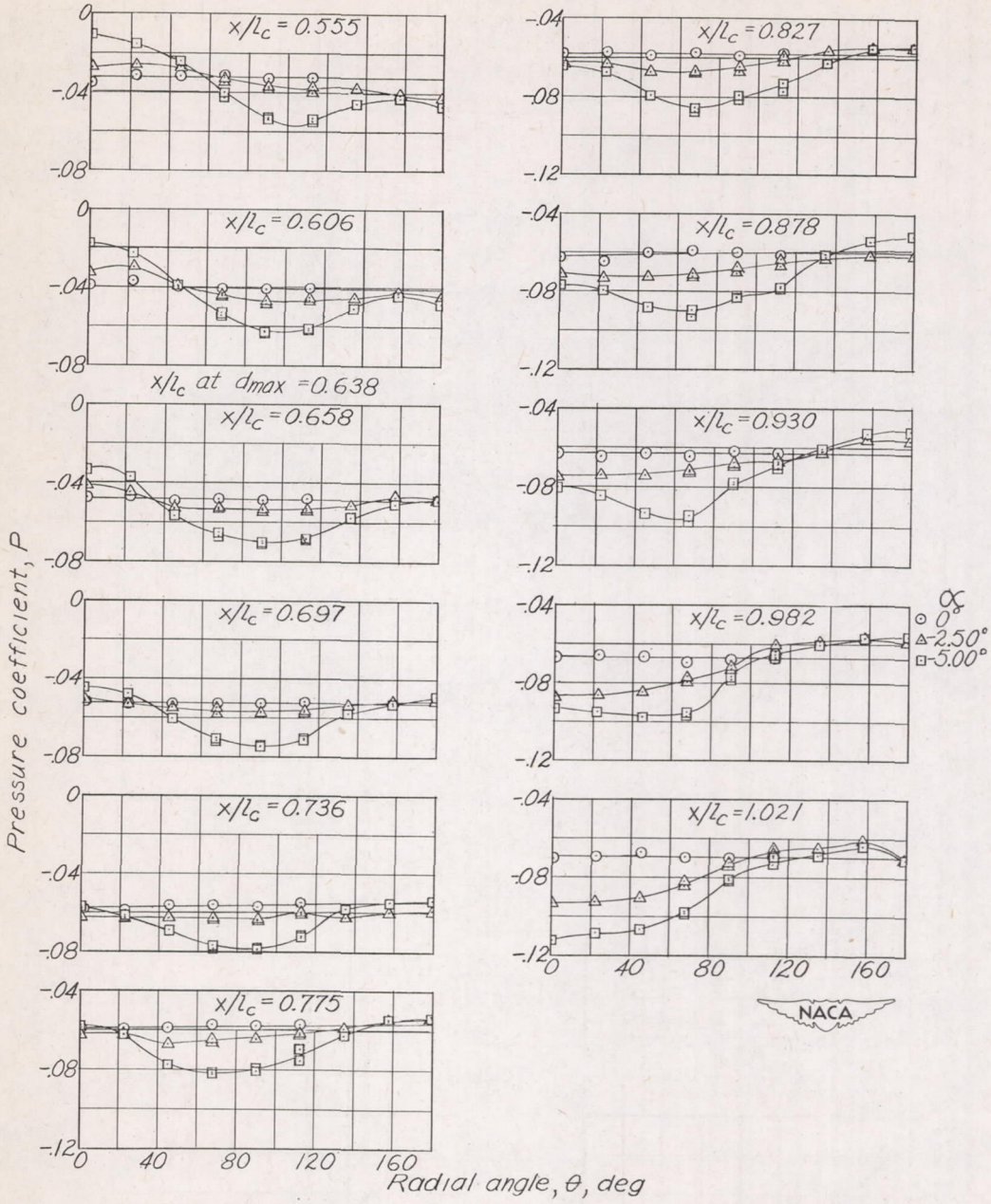

Figure 10.- Concluded.

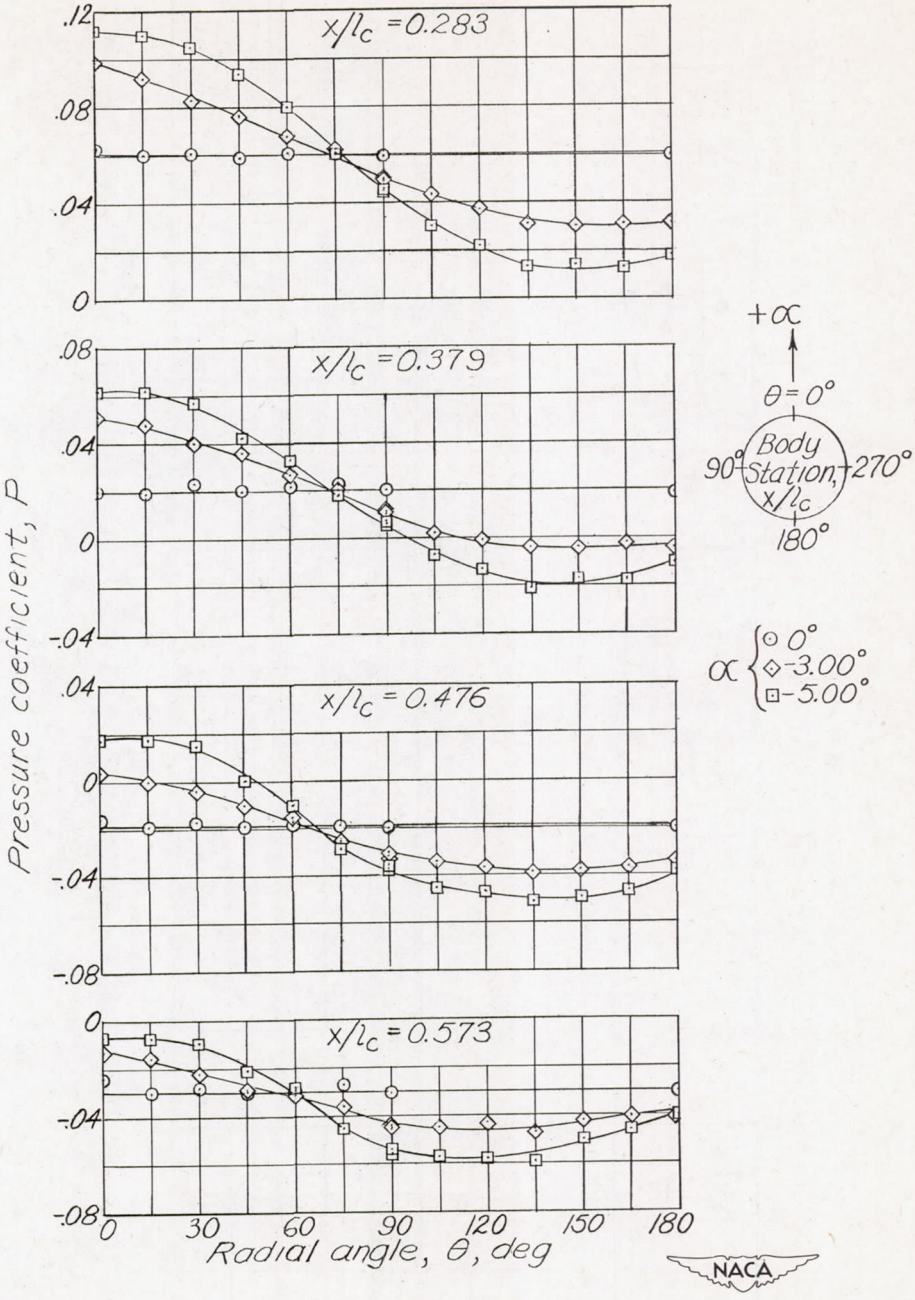

(a) Body stations ahead of maximum thickness station.

Figure 11.- Radial pressure distributions for model 2.

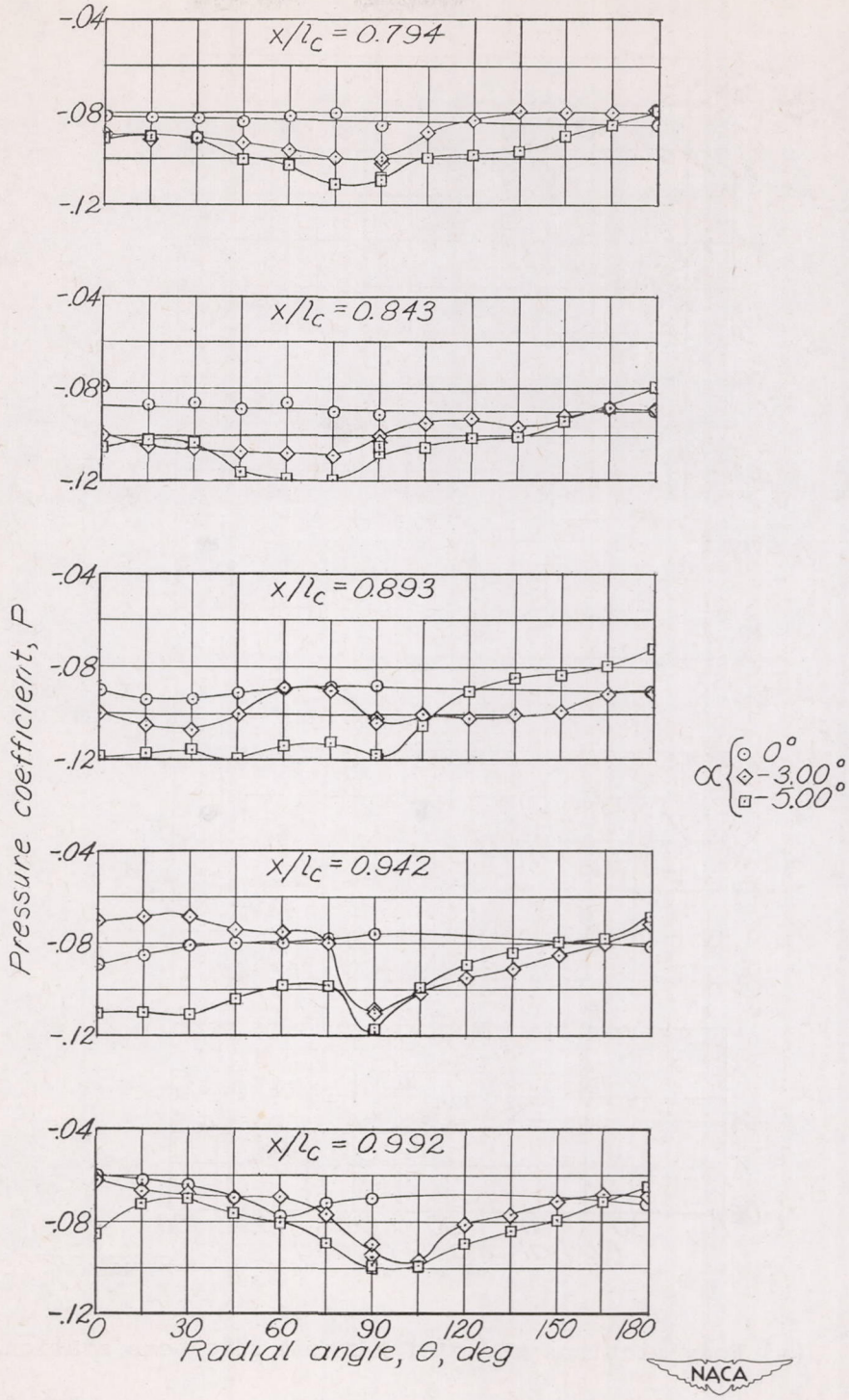

(b) Body stations behind maximum thickness station.

Figure 11.- Concluded.

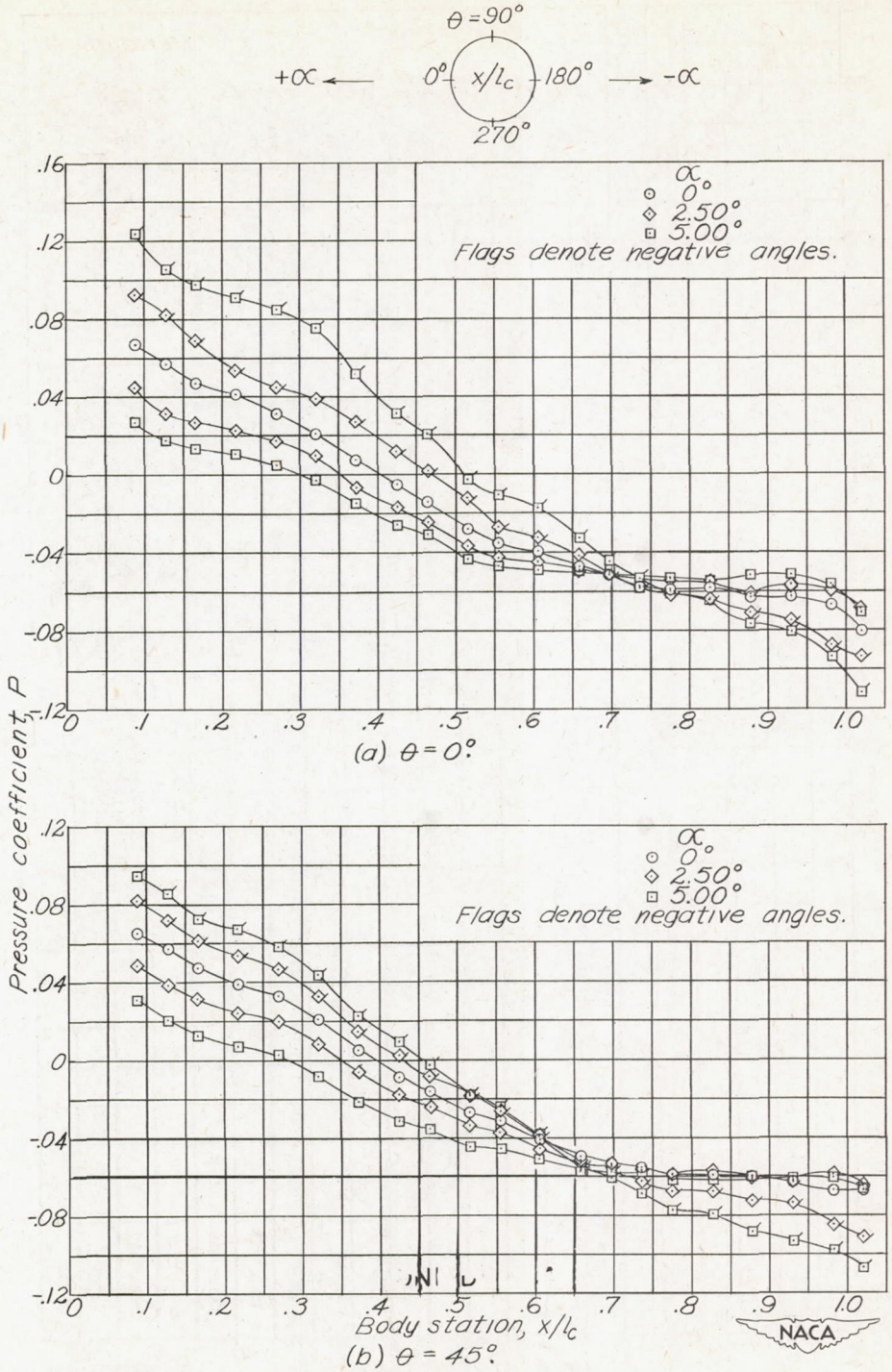

Figure 12.- Variation of longitudinal pressure distribution with angle of attack at two meridians of model 1-P.

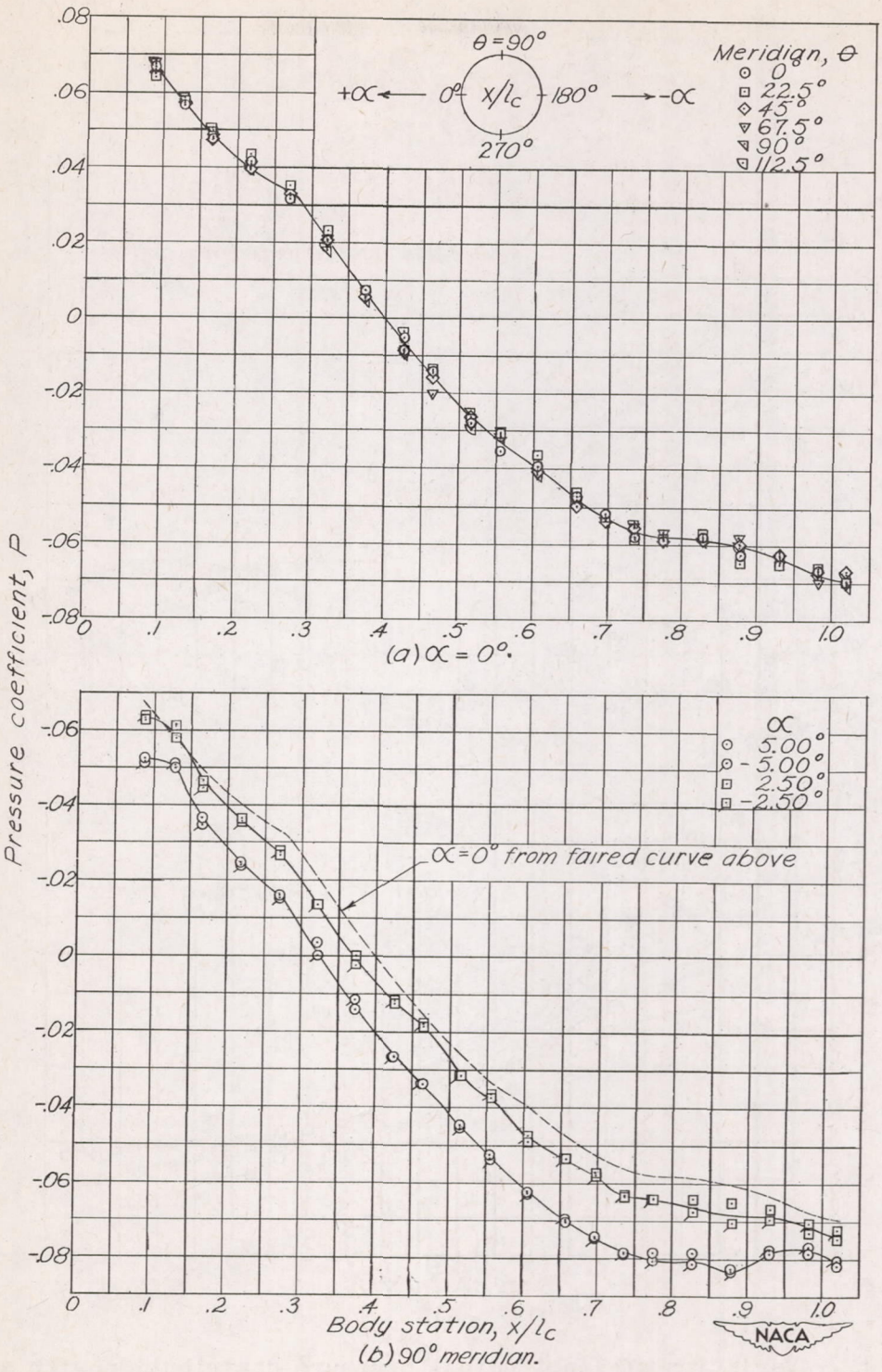

Figure 13.- Longitudinal pressure distribution of model 1-P at $\alpha = 0^{\circ}$ and variation of 90° meridian pressures with angle of attack.

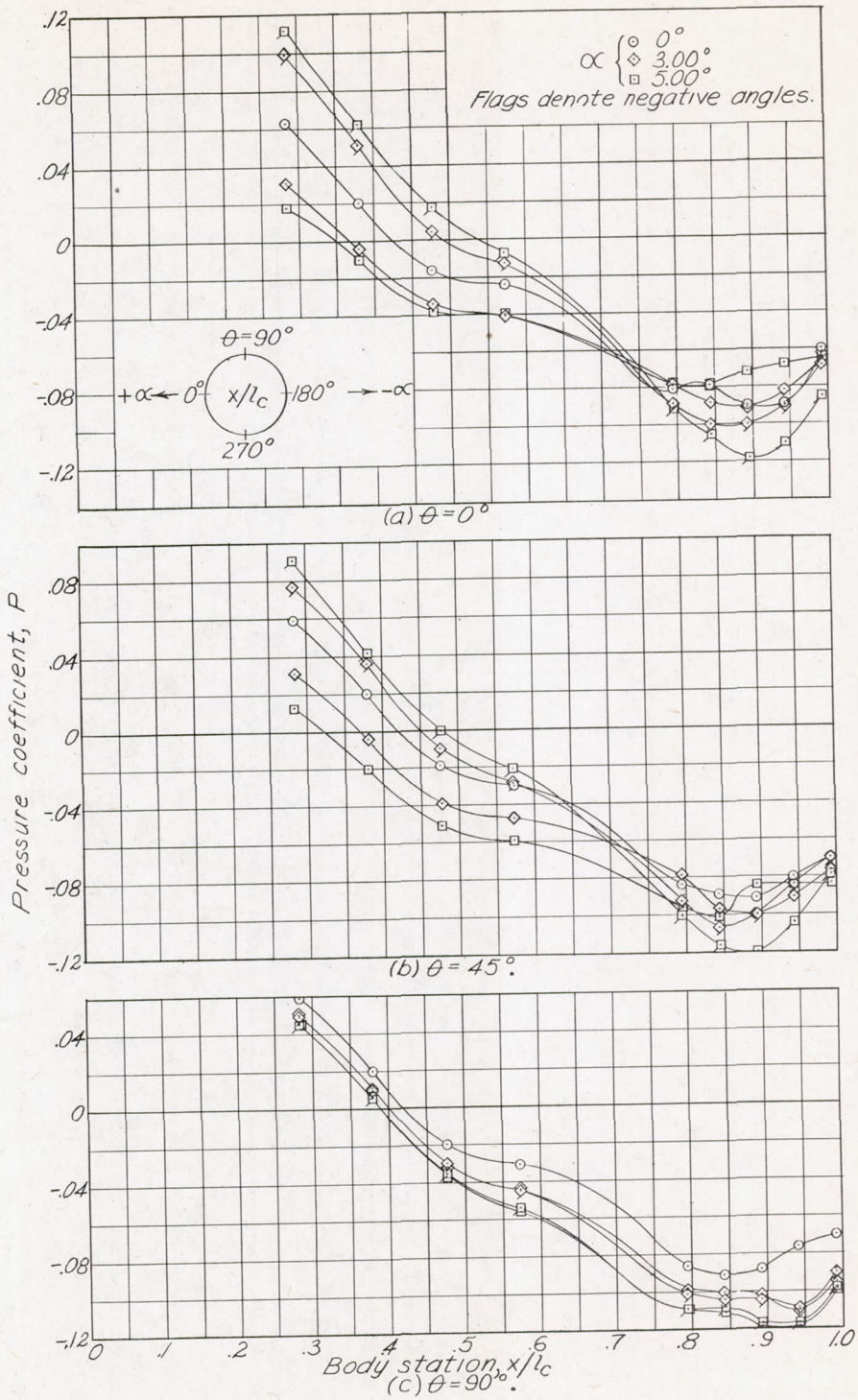

Figure 14.- Longitudinal pressure distributions for model 2.

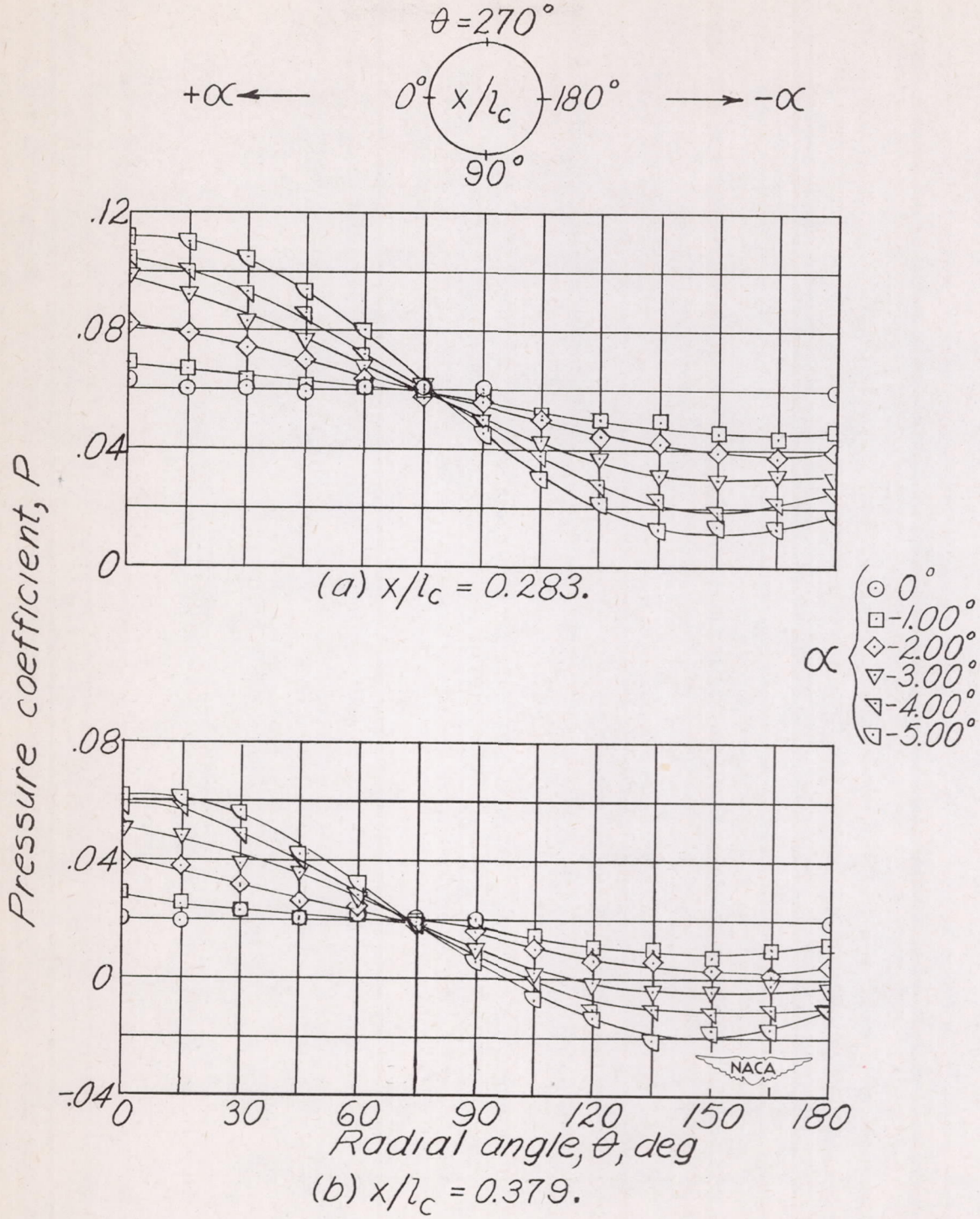

Figure 15.- Radial pressure distributions for model 2. (Examples of radial point of zero pressure variation with angle of attack.)

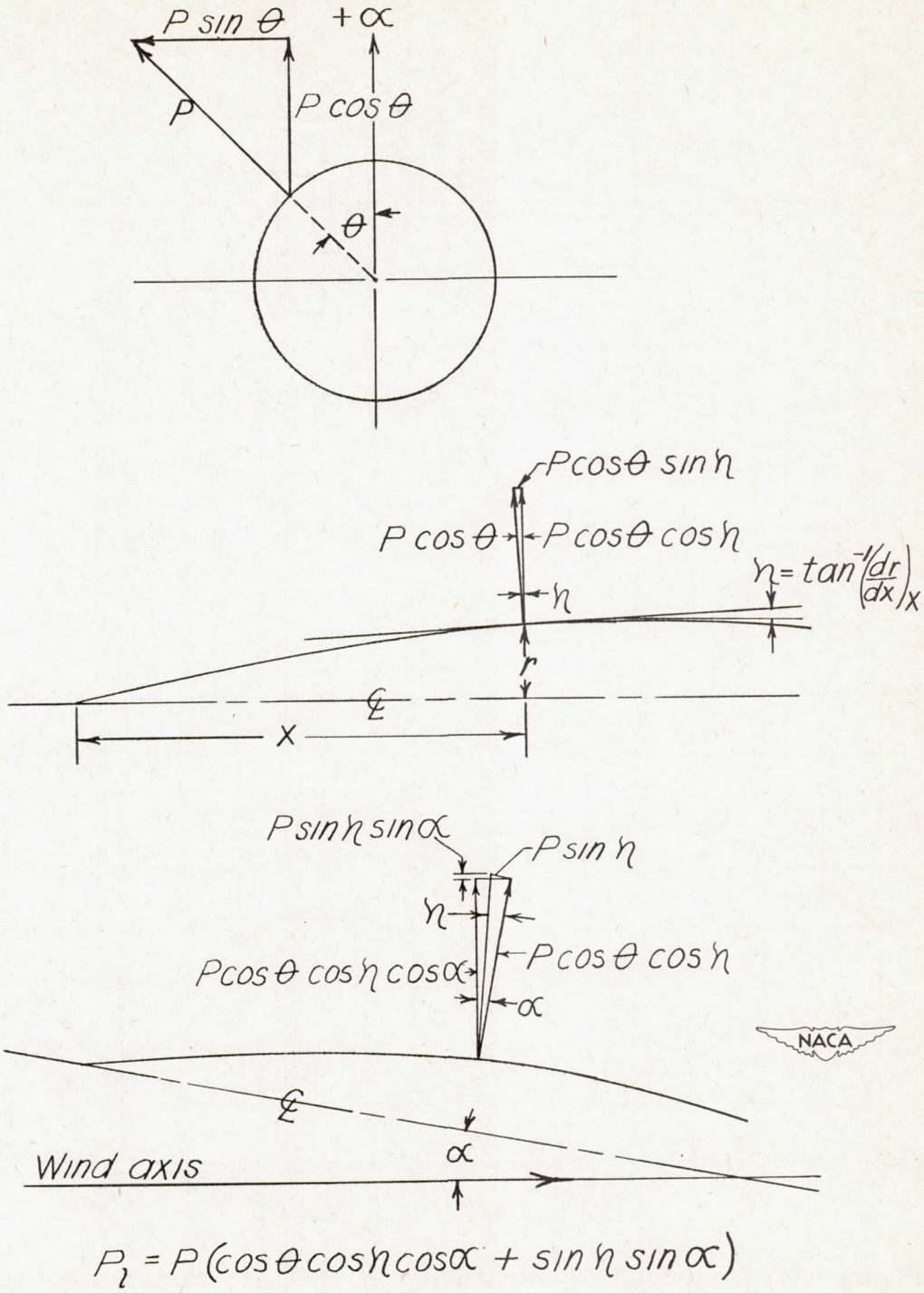

Figure 16.- Conversion of normal pressures to lifting pressures.

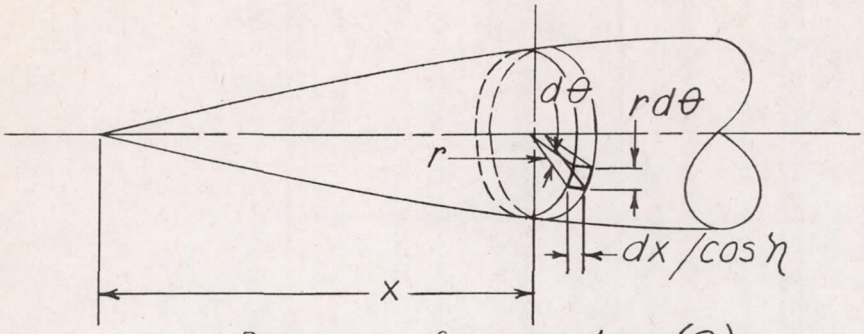

Diagram for equation (8)

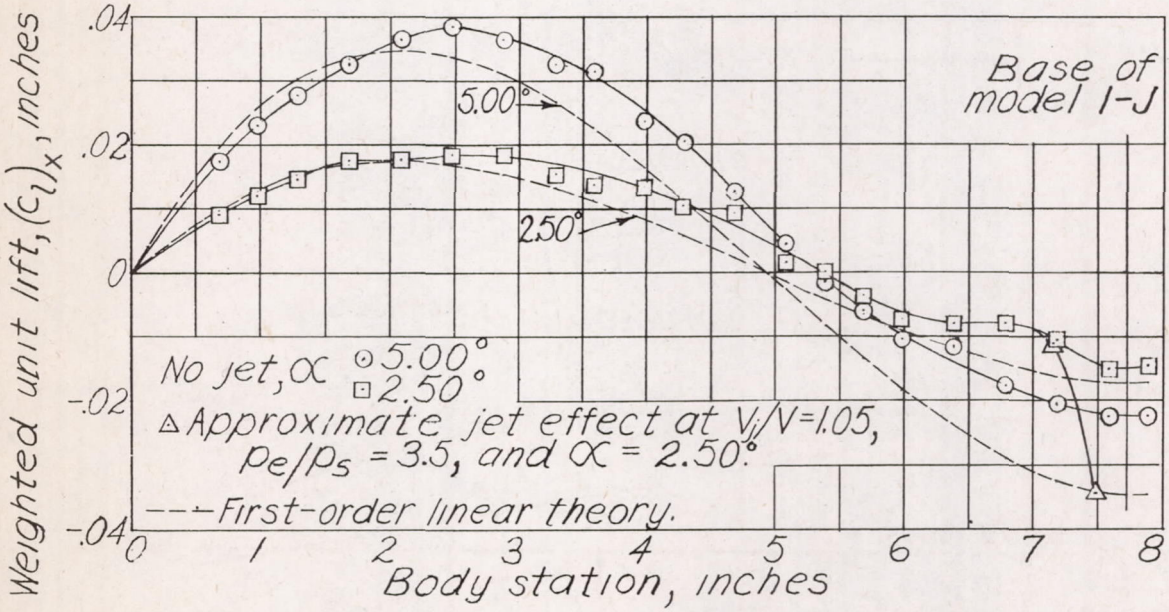

Figure 17.- Graphical representation of the lift distribution over model 1-P.

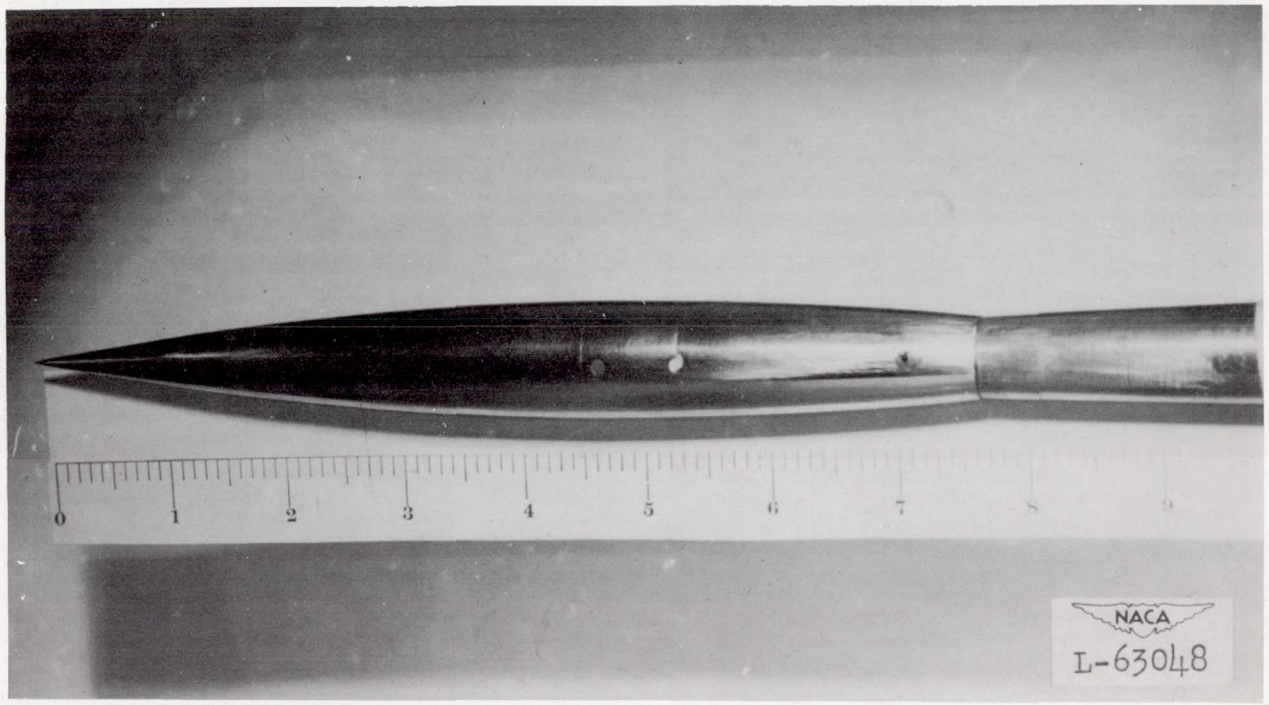

Figure 18.- Model 1-F with flush sting windshield.

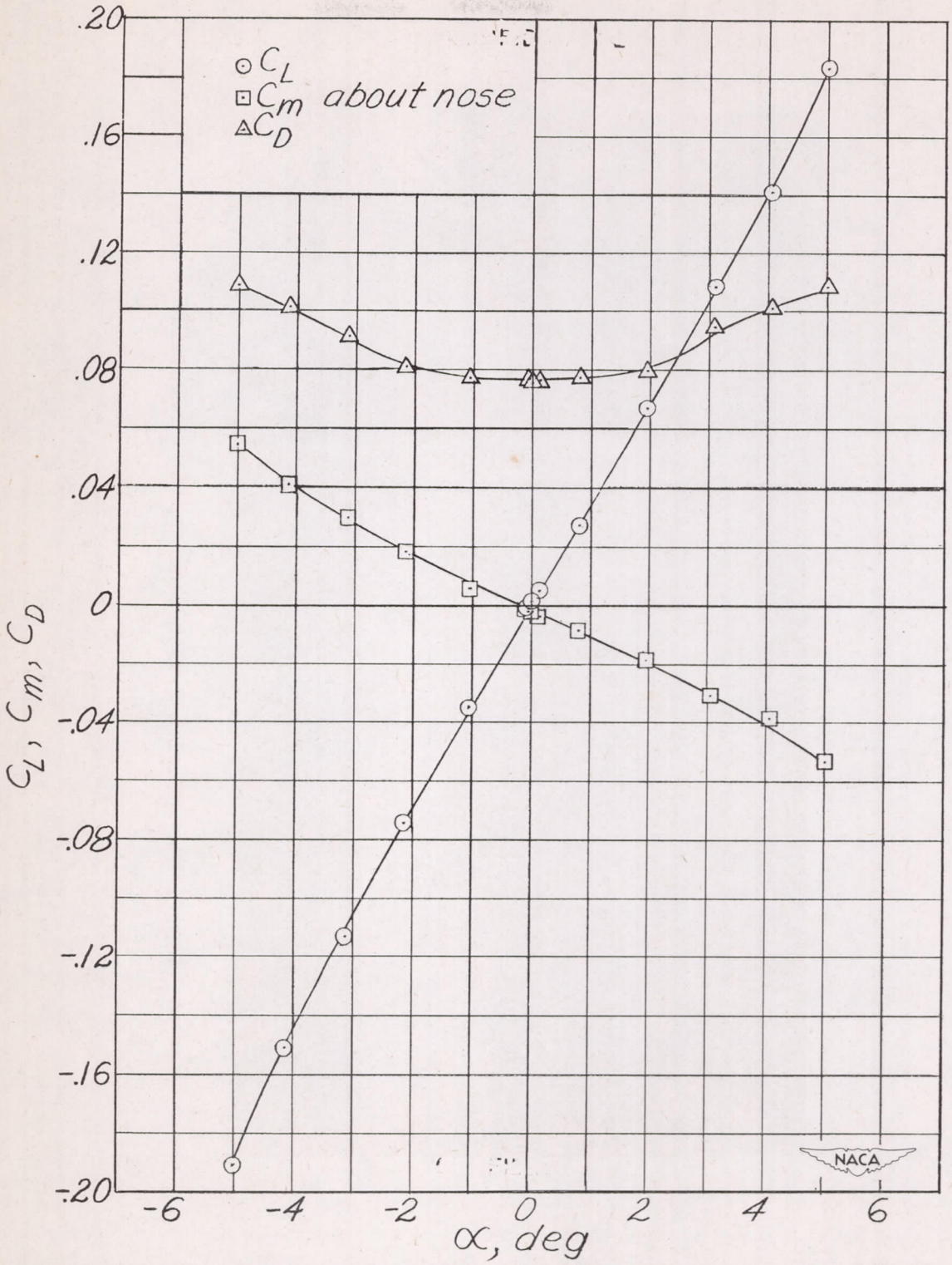

Figure 19.- Aerodynamic characteristics of model 1-F; surface of sting windshield flush with body base.

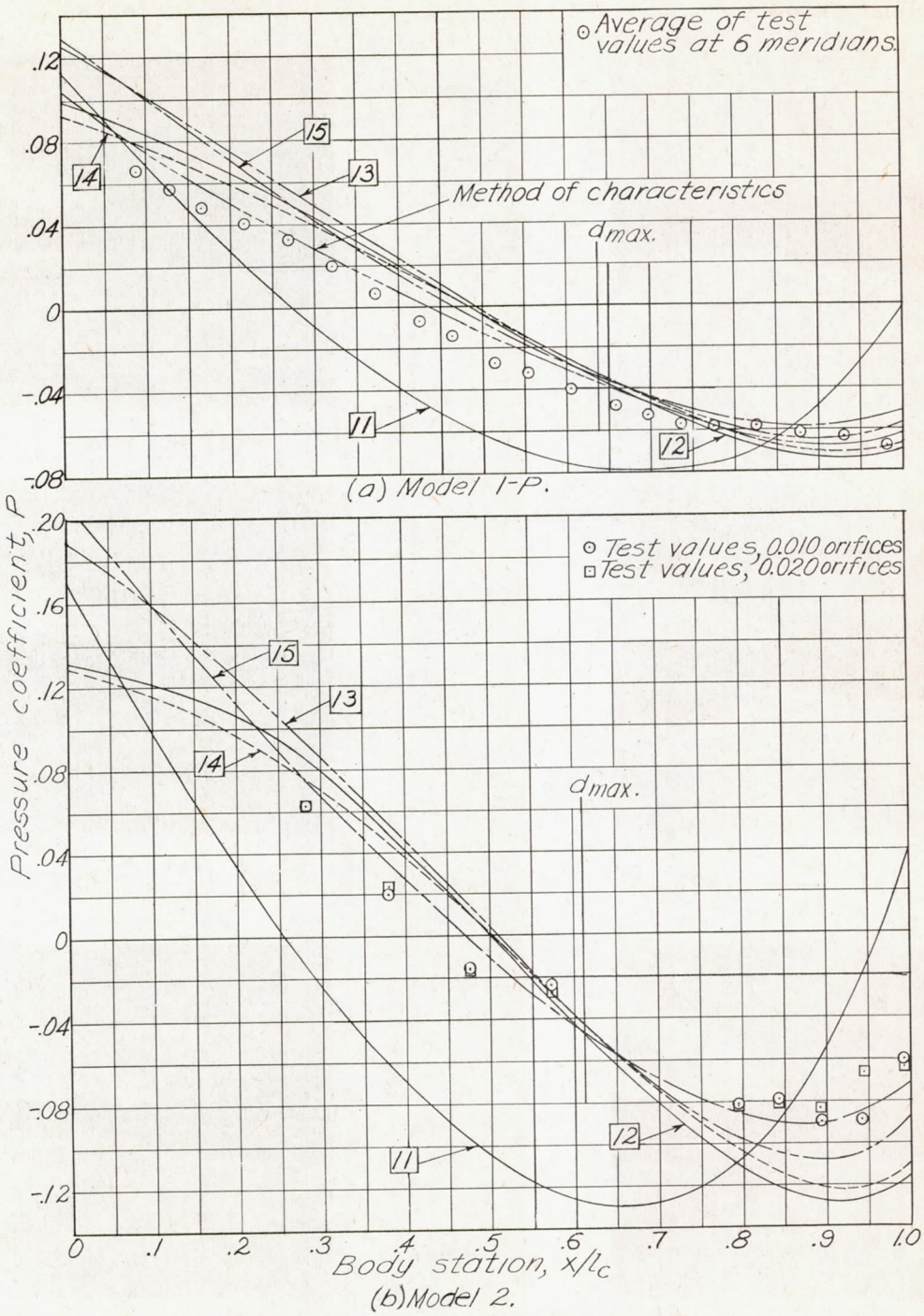

Figure 20.- Comparison of theoretical and experimental pressure distributions for $\alpha = 0^{\circ}$. (Numbers in squares indicate equation numbers in text.)

Without pressure lead tubes

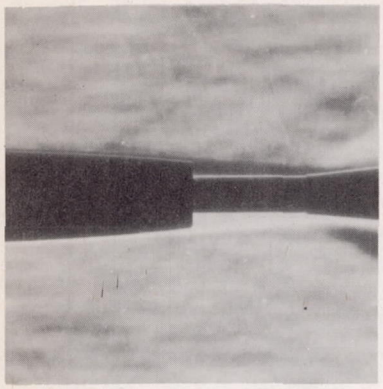

(a) No jet.

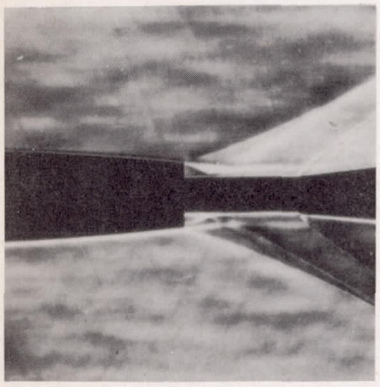

(b) $\frac{p_e}{p_s} = 0.427.$

(c) $\frac{p_e}{p_s} = 1.71.$

Pressure lead tubes installed

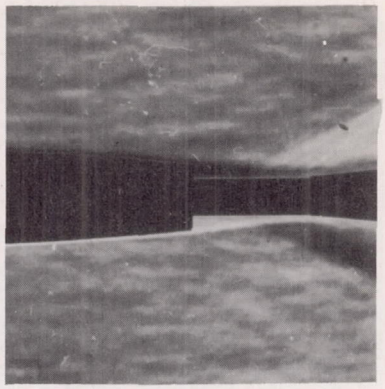

(a) No jet.

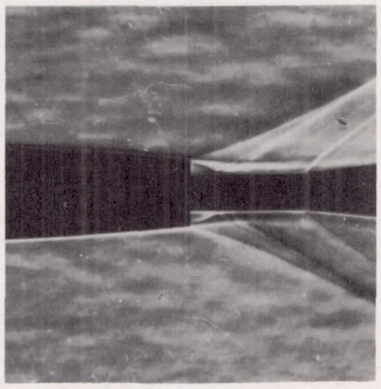

(b) $\frac{p_e}{p_s} = 0.429.$

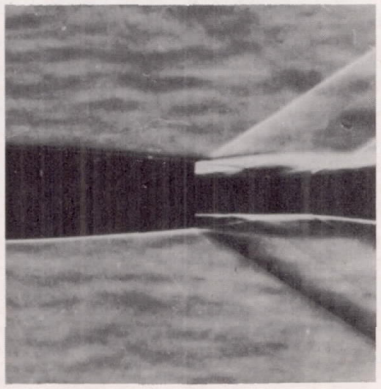

(c) $\frac{p_e}{p_s} = 1.70.$

NACA
L-63044

Figure 21.- Schlieren photographs of phenomena at jet exit without and with pressure lead tubes installed; $\frac{V_j}{V} = 1.24.$

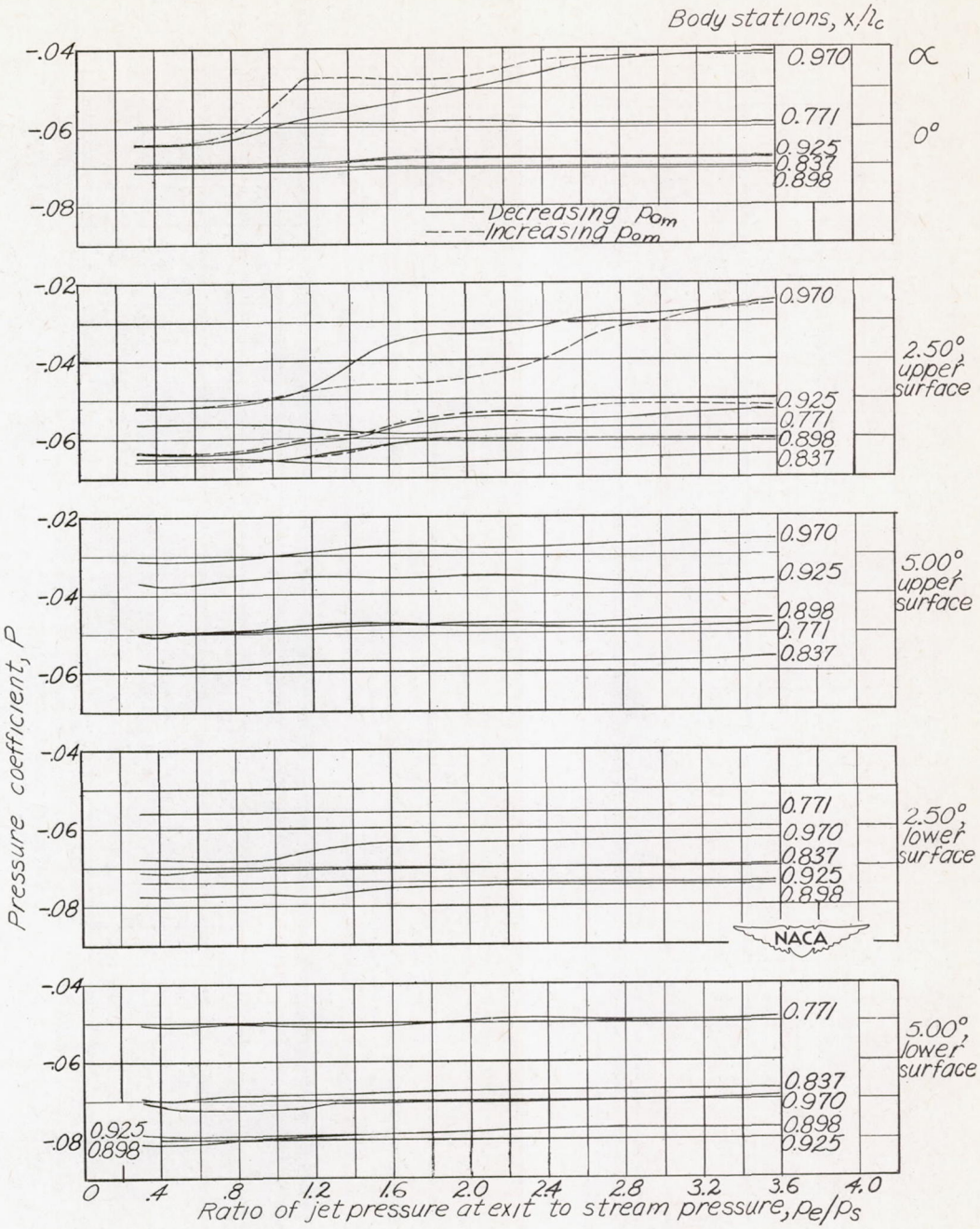

(a) $\frac{V_j}{V} = 1.05.$

Figure 22.- Effects of jet upon pressures at rear body stations with varying angle of attack and jet pressures.

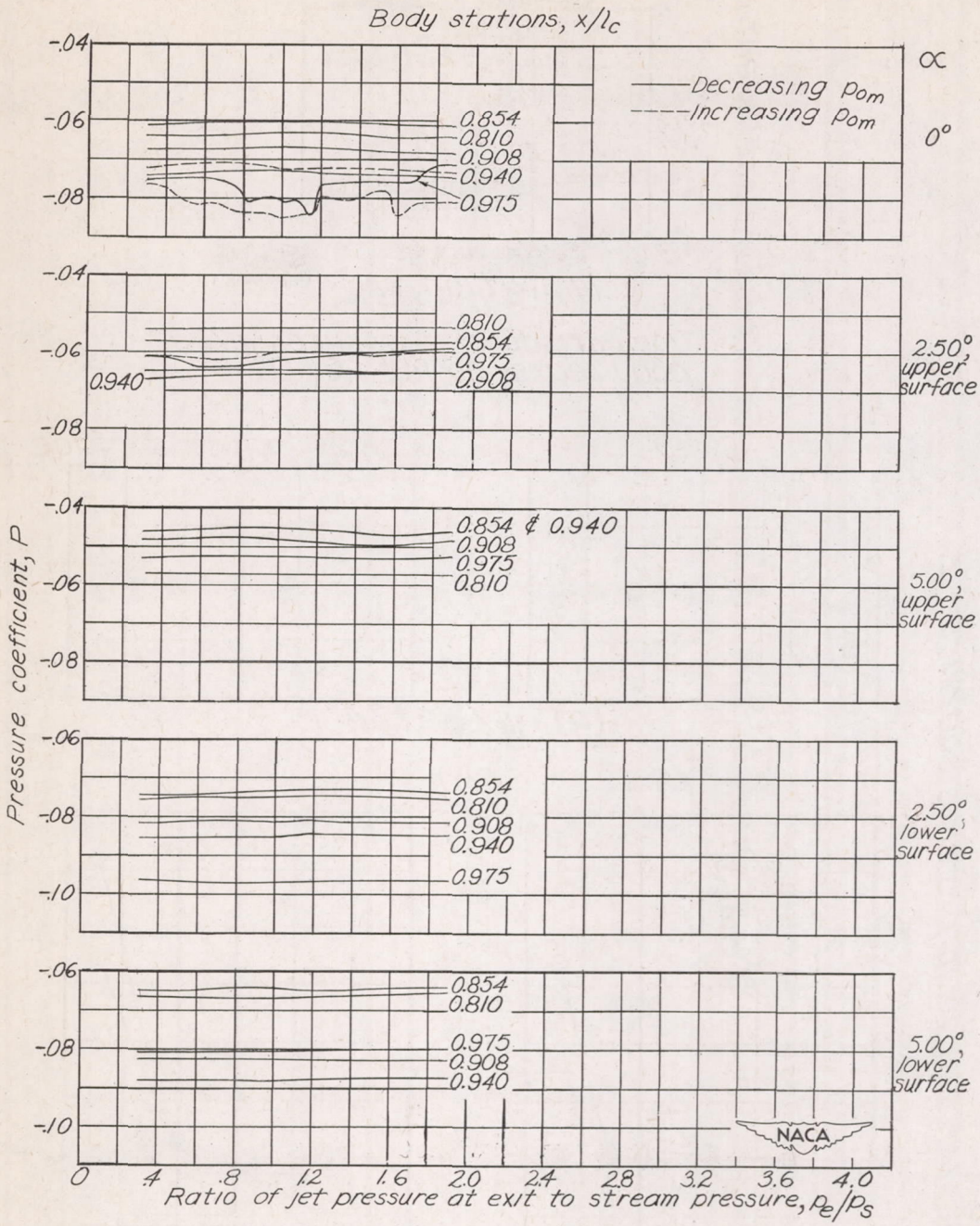

(b) $\frac{V_j}{V} = 1.24$.

Figure 22.- Concluded.

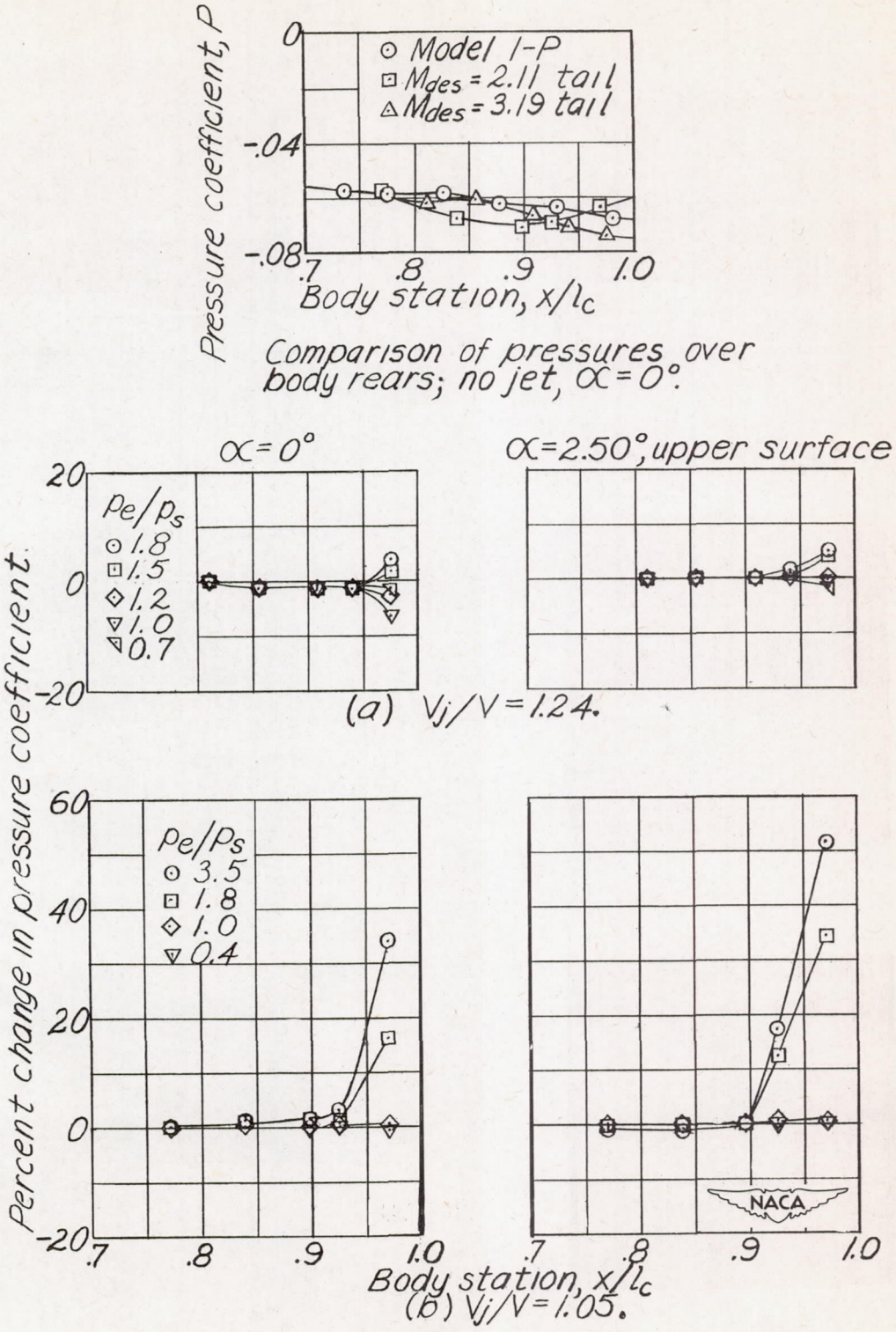

Figure 23.- Effects of jet upon rear body pressures.

$\frac{V_j}{V} = 1.05.$

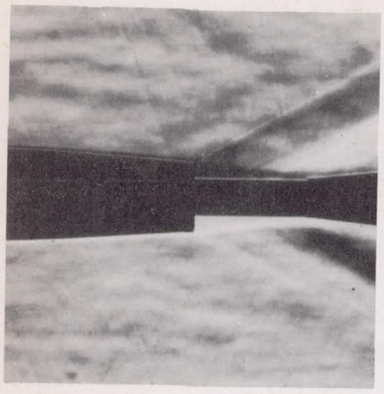

(a) No jet.

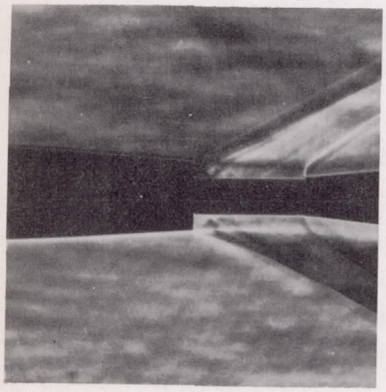

(b) $\frac{p_e}{p_s} = 0.390.$

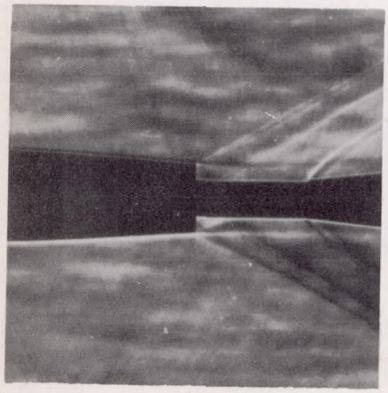

(c) $\frac{p_e}{p_s} = 0.638.$

$\frac{V_j}{V} = 1.24.$

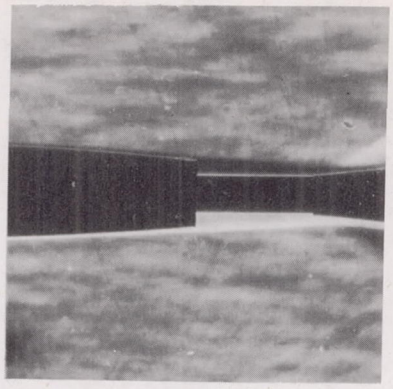

(a) No jet.

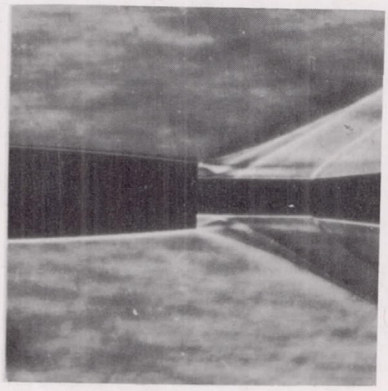

(b) $\frac{p_e}{p_s} = 0.404.$

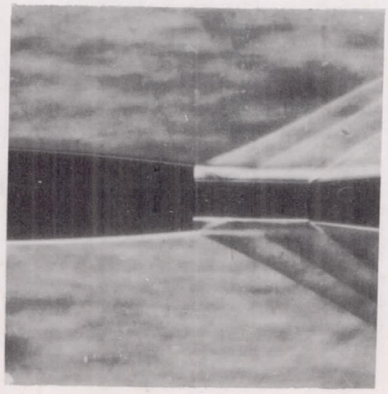

(c) $\frac{p_e}{p_s} = 0.611.$

NACA
L-63045

Figure 24.- Schlieren photographs of jet in operation at two ratios of jet velocity to free-stream velocity and with varying ratios of jet pressure to free-stream pressure. $\alpha = 0^{\circ}$.

$\frac{V_j}{V} = 1.05.$

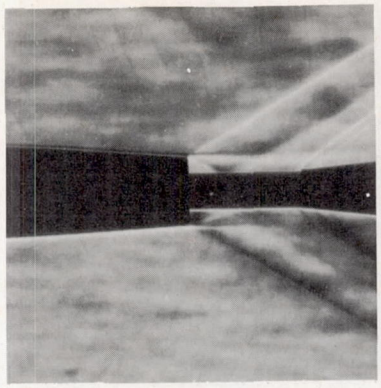

(d) $\frac{p_e}{p_s} = 1.103.$

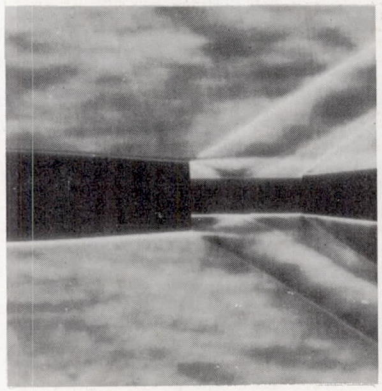

(e) $\frac{p_e}{p_s} = 1.325.$

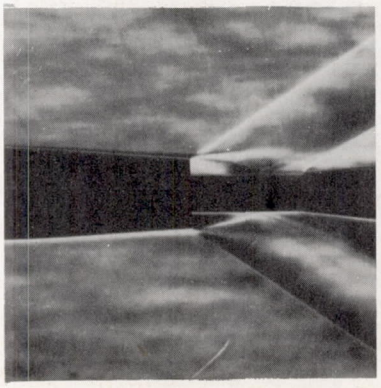

(f) $\frac{p_e}{p_s} = 2.018.$

$\frac{V_j}{V} = 1.24.$

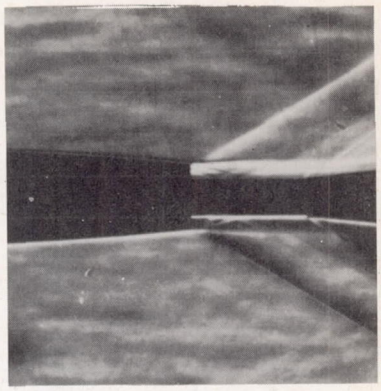

(d) $\frac{p_e}{p_s} = 1.100.$

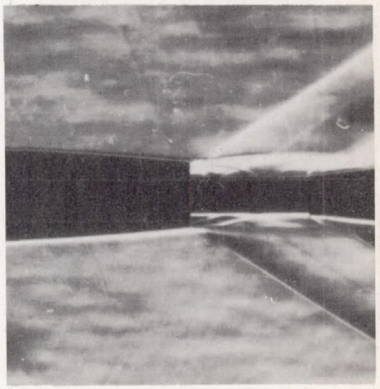

(e) $\frac{p_e}{p_s} = 1.381.$

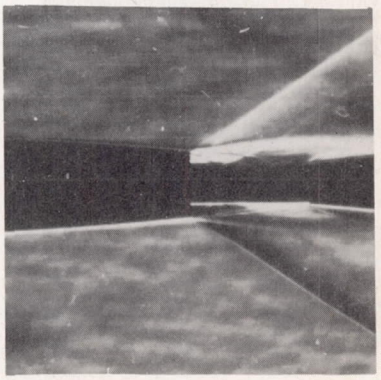

(f) $\frac{p_e}{p_s} = 2.100.$

NACA
L-63046

Figure 24.- Continued.

$\frac{V_j}{V} = 1.05.$

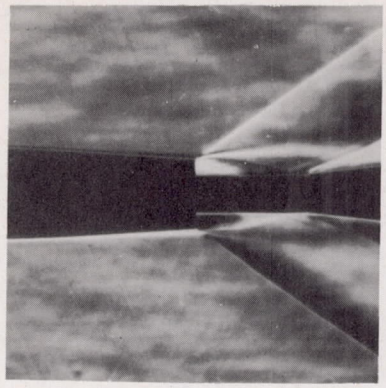

(g) $\frac{p_e}{p_s} = 2.704.$

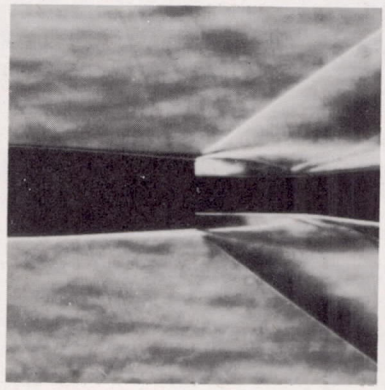

(h) $\frac{p_e}{p_s} = 3.157.$

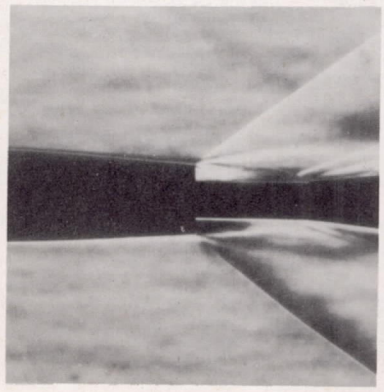

(i) $\frac{p_e}{p_s} = 3.620.$

NACA
L-63047

Figure 24.- Concluded.

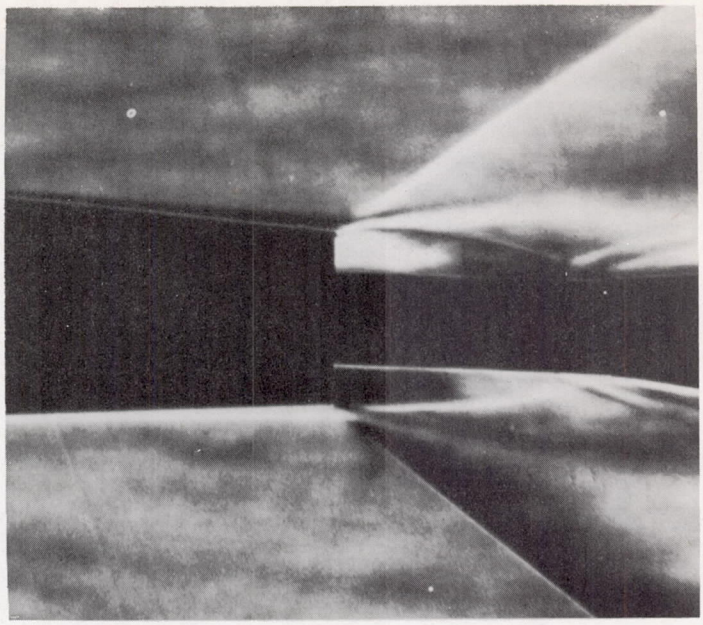

L-93528

(a) Schlieren photograph of flow phenomena.

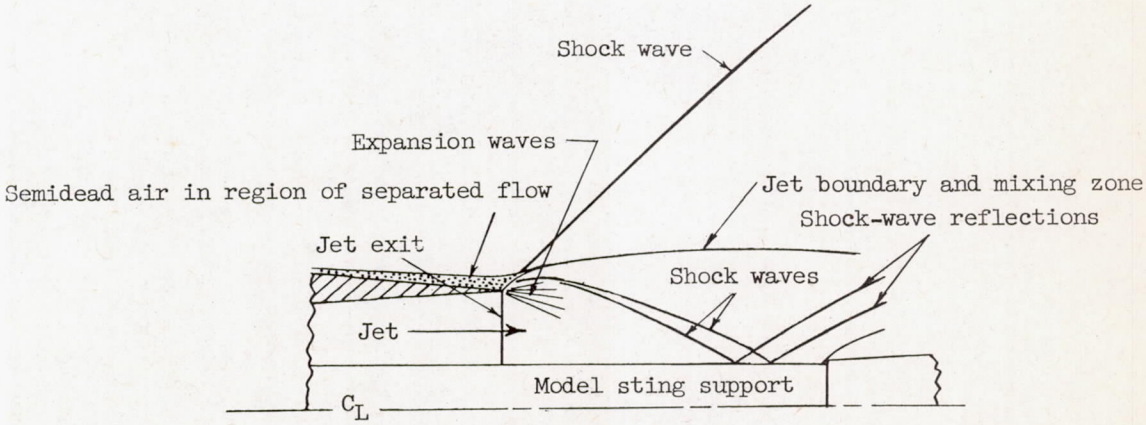

(b) Sketch of flow phenomena.

Figure 25.– Phenomena in region of jet exit; $\frac{V_j}{V} = 1.05$, $\frac{p_e}{p_s} = 3.16$.